

Elastic disk with isoperimetric Cosserat coating

Matteo Gaibotti ¹, Davide Bigoni ^{*1}, and Sofia G. Mogilevskaya ²

¹DICAM, University of Trento, via Mesiano 77, I-38050 Trento, Italy

²Departement of Civil, Environmental and Geo- Engineering, University of Minnesota, 500 Pillsbury Drive S.E. Minneapolis, MN 55455-0116, USA.

e-mail: matteo.gaibotti@unitn.it, bigoni@ing.unitn.it, mogil003@umn.edu

Dedicated to

Professors Natasha and Sasha Movchan on the occasion of their 60th birthday

Abstract

A circular elastic disk is coated with an elastic beam, absorbing shear and normal forces without deformation and linearly reacting to a bending moment with a change in curvature. The inextensibility of the elastic beam introduces an isoperimetric constraint, so that the length of the initial circumference of the disk is constrained to remain fixed during the loading of the disk/coating system. The mechanical model for this system is formulated, solved for general loading, and particularized to the case of two equal and opposite traction distributions, each applied on a small boundary segment (thus modelling indentation of a coated fiber). The stress fields, obtained via complex potentials, are shown to evidence a nice correspondence with photoelastic experiments, *ad hoc* designed and performed. The presented results are useful for the design of coated fibers at the micro and nano scales.

1 Introduction

Several technologies involve coating of the surface of a bulk material with a thin layer made up of another material. This technique was developed in order to enhance electrical conductivity [1, 2, 3], achieve electrical insulation [4, 5], protect from heating [6, 7], enhance biocompatibility [8, 9, 10], increase strength [11] or wear, fatigue, or corrosion resistance [12].

A coating layer diffuses the load on an attached solid in a nonlocal way, introduces a characteristic length, and deeply affects the mechanics of the coated object. As a consequence, a strong research effort has been devoted to the modelling of coatings and to the analysis of associated problems. In the framework of the nonlinear theory of

^{*}Corresponding author: Davide Bigoni fax: +39 0461 282599; phone: +39 0461 282507; web-site: <http://www.ing.unitn.it/~bigoni/>; e-mail: bigoni@ing.unitn.it.

elasticity, the coating may be modelled as a surface possessing a membrane stiffness [13], possibly enhanced with a flexural and torsional stiffness [14, 15]. Applications of these theories have been presented to bifurcation [16, 17] and wave propagation [18] in coated elastic blocks.

Within the realm of linear elasticity, the coating has been idealized as an elastic shell (becoming a curved beam in a two-dimensional formulation) [19, 20]. In composites, the presence of a film separating two elastic media has been reduced to a thin interface, suitably describing the contact conditions. This interface model has been used to estimate the effective mechanical properties of composites with inclusions [21, 19, 22] and for applications in thermal conductivity [23].

The advent of nanotechnologies has strongly fueled the development of interface models. These have been used to estimate thermo-mechanical properties of nano-composites, of mono-layered-graphene based materials [24, 25], to analyze the interaction between nano- inhomogeneities [26] and the mechanics of reinforcements, such as coated fibers [27, 28] or nanoplatelets embedded in a core matrix [29, 30]. The presence of coatings or thin layers strongly influences failure mechanisms, such as crack nucleation and propagation inside the coating/substrate [31, 32, 33], or delamination induced by mechanical/thermal mismatch and residual stresses existing between coating and substrate [34, 35, 36, 37, 38, 39, 40, 41, 42], or by curvature changes or buckling [43, 44, 45].

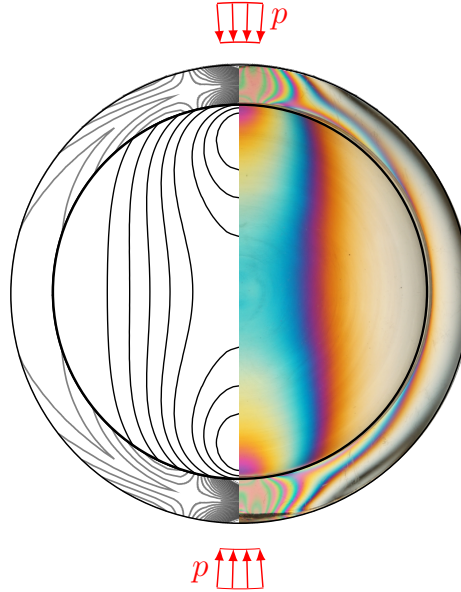


Figure 1: Qualitative comparison between the in-plane deviatoric stress ($|\sigma_I - \sigma_{II}|/\mu$, analytically evaluated with the disk/coating model introduced in the present article) and the photoelastic fringes resulting during a diametral compression test of a coated disk. The sample before testing is reported in the upper part of Fig. 5. The applied external load distribution p is modelled with a Fourier series expansion, enhanced with the Lanczos smoothing method (Section 4.2.1).

In the present article a circular disk made up of a (linear, isotropic) elastic material is analyzed, covered with a ‘beam-like’ model of coating, of the type introduced by Benveniste and Miloh [20]. The beam model is assumed to satisfy inextensibility, so that an isoperimetric constraint is introduced of the Cosserat type, as the beam transmits

bending¹. The cylindrical geometry considered here may be important in view of the development of nanowire technology (where a coated cylinder is obtained, when a nanowire is grown inside a single-wall carbon nanotube [46]). We show that, when the exterior of the coated disk is loaded by a generic (but self-equilibrated) force distribution, the problem can be analytically solved via complex potentials, thus obtaining the displacement, strain, and stress fields within the disk, together with the axial and shear forces and bending moment in the coating.

The analytical result is complemented with the explicit treatment of the case in which the coating/disk system is subject to a load distribution modelling two equal and opposite concentrated forces. This load corresponds to that applied during a nanoindentation test (often performed on nanofibers to measure their mechanical properties [47]) and may easily be reproduced experimentally. On this vein, we have designed two coated disks, manufactured (with a CNC engraving machine) from a single block of polymethyl methacrylate, so that the bonding between the coating and disk is perfect and residual stresses are absent. The samples have been tested in a circular polariscope and the results strongly support the coated disk model, so that the photoelastic fringes are very well captured by the elastic solution, as anticipated in Fig. 1. The figure shows the strong effect of the coating, where the stress distribution is typical of that forming inside a curved beam subject to bending moment.

The article is organized as follows. After the coating/disk system is modelled in Section 2, the equations governing its behaviour are presented (Section 3). The special case of loading consisting of two equal and opposite radial force distributions applied to a small area is solved in Section 4.1 and the solution is compared with photoelastic experimental results in Section 4.3.

2 Modelling of the complex coating/disk

A (linear and isotropic) elastic circular disk is examined, enclosed in a perfectly-bonded annular elastic beam, which obeys the Euler-Bernoulli model, so that it is axially inextensible, unshearable and reacts linearly to a curvature variation through the development of a bending moment. The mechanical model of the coating/disk system follows from the combination of the separate equations holding for its two components, which are introduced below.

2.1 The coating, a circular annular beam

A circular Euler-Bernoulli (unshearable) elastic beam of bending stiffness EJ and radius R is considered. The center of the circle is located at the origin of the Cartesian coordinate system with axes x_1 and x_2 and the polar system r and θ (the latter assumed positive when counterclockwise), equipped with the two radial and circumferential unit vectors \mathbf{e}_r and \mathbf{e}_θ (Fig. 2). The beam is subjected to radial and tangential forces, respectively p and q , that will be applied by both the external environment and the elastic disk. The internal forces along the beam, comprised of normal and shear components, N and T , as

¹More precisely, an Euler-Bernoulli beam is an example of constrained Cosserat material, whereas a Timoshenko beam corresponds to the unconstrained Cosserat case, called also micropolar unconstrained theory.

well as bending moment M , satisfy *equilibrium*

$$\frac{dN}{ds} + \frac{T}{R} = -q, \quad -\frac{dT}{ds} + \frac{N}{R} = -p, \quad \frac{dM}{ds} = -T, \quad (1)$$

where $ds = R d\theta$ is the elementary arclength defined anticlockwise accordingly with θ .

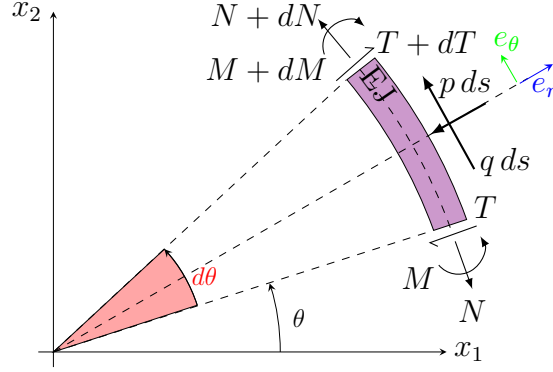


Figure 2: The coating of the disk is modelled with an inextensible and unshearable elastic beam (with bending stiffness EJ). The beam introduces an isoperimetric closed contour L , so that the perimeter of the coating cannot change its total volume, when a load of components p (radial) and q (tangential) is applied. This load generates internal normal and shear forces, N and T , and bending moment M .

The *kinematics* of the beam is defined by a radial u_r and tangential u_θ displacement and a rotation Φ , the latter positive when clockwise. Pure kinematic considerations, sketched in Fig. 3, show that the axial deformation ϵ , the rotation Φ , and the curvature χ (the latter additional and opposite to the natural curvature $1/R$ of the circle) are given by [48]

$$\epsilon = \frac{u_r}{R} + \frac{du_\theta}{ds}, \quad \Phi = -\frac{u_\theta}{R} + \frac{du_r}{ds}, \quad \chi = -\frac{d\Phi}{ds}. \quad (2)$$

The beam represents an example of constrained Cosserat solid, capable of reacting to a change in curvature with a bending moment according to the linear *constitutive equation*

$$\chi = -\frac{M}{EJ}. \quad (3)$$

It is assumed now that this beam be *axially inextensible*, so that $\epsilon = 0$, namely,

$$\frac{du_\theta}{d\theta} = -u_r, \quad (4)$$

a relation which introduces a local isoperimetric constraint for the area enclosed inside the annular region, which perimeter cannot change. Here, differently from the mathematical ‘Queen Dido problem’, the curve enclosing the area is an elastic beam, equipped with a finite bending stiffness and subjected to external loads.

Equations (1)–(3), determining the mechanics of an annular beam under quasi-static loading, can now be particularized for the inextensibility constraint $\epsilon = 0$ to hold, so that they become functions of the radial displacement u_r only, as follows.

- Kinematics governing the displacements and rotation, u_r , u_θ , and Φ :

$$u_\theta = -\int u_r(\theta) d\theta, \quad R\Phi = -u_\theta + \frac{du_r}{d\theta}, \quad \chi = -\frac{1}{R} \frac{d\Phi}{d\theta}. \quad (5)$$

- Constitutive equations for the internal forces M , T , and N :

$$\begin{aligned}\frac{M}{EJ} &= \frac{d^2 u_r}{ds^2} + \frac{u_r}{R^2}, \\ \frac{T}{EJ} &= -\frac{d^3 u_r}{ds^3} - \frac{1}{R^2} \frac{du_r}{ds}, \\ \frac{N}{EJ} &= -R \left(\frac{d^4 u_r}{ds^4} + \frac{1}{R^2} \frac{d^2 u_r}{ds^2} + \frac{p}{EJ} \right).\end{aligned}\tag{6}$$

- Differential equation for the radial displacement u_r :

$$\frac{d^5 u_r}{d\theta^5} + 2 \frac{d^3 u_r}{d\theta^3} + \frac{du_r}{d\theta} = \frac{R^4}{EJ} \left(q - \frac{dp}{d\theta} \right).\tag{7}$$

Equations (4) and (7) define the so-called *inextensional shell type* interface model introduced by Benveniste and Miloh [20], their equations (2.15)₃ and (2.15)₄ with $N = 3$, in the particular case when the radius of curvature is constant. More in detail, equation (4.9) in [20] coincides with the above equation (7).

2.2 The coated disk

A two-dimensional (thus subject to conditions of either plane stress or plane strain) elastic disk of radius R , made up of an isotropic material (defined by a shear modulus μ and Poisson's ratio ν), is coated with the above introduced beam (Euler-Bernoulli, axially inextensible and unshearable, Fig. 4). The coating is perfectly connected to the disk and hence conditions of continuity of displacement at the contact between the two impose the following conditions

$$u_r^{(b)} = u_r^{(d)}|_{r=R}, \quad u_\theta^{(b)} = u_\theta^{(d)}|_{r=R},\tag{8}$$

where (b) and (d) denote the ‘beam’ and the ‘disk’, respectively. These superscripts will be in the following avoided, as the distinction between the two will be not needed, as they have been assumed to coincide.

The axial inextensibility of the coating enforces the isoperimetric constraint (5)₁ on the points of the boundary L of the disk

$$u_\theta = -\frac{1}{R} \int_L u_r ds,\tag{9}$$

defining a *nonlocal relation* between displacement components.

The load on the coating, of components p and q in equations (1)_{1,2}, (6)₃, and (7), is partially applied externally to the disk, but also transmitted by the disk in terms of stress components σ_{rr} and $\sigma_{r\theta}$ (multiplied by the thickness of the disk b , which becomes unity in a plane strain problem). Therefore, the loads p and q present in equations (1)_{1,2}, (6)₃, and (7), have now to be interpreted as

$$q \longrightarrow q - b\sigma_{r\theta}, \quad \text{and} \quad p \longrightarrow p + b\sigma_{rr},\tag{10}$$

so that in this way p and q are identified as external loads applied to the coated disk. In a complex notation, the total load applied on the coating can be represented as

$$P = p + b\sigma_{rr} + i (q - b\sigma_{r\theta}).\tag{11}$$

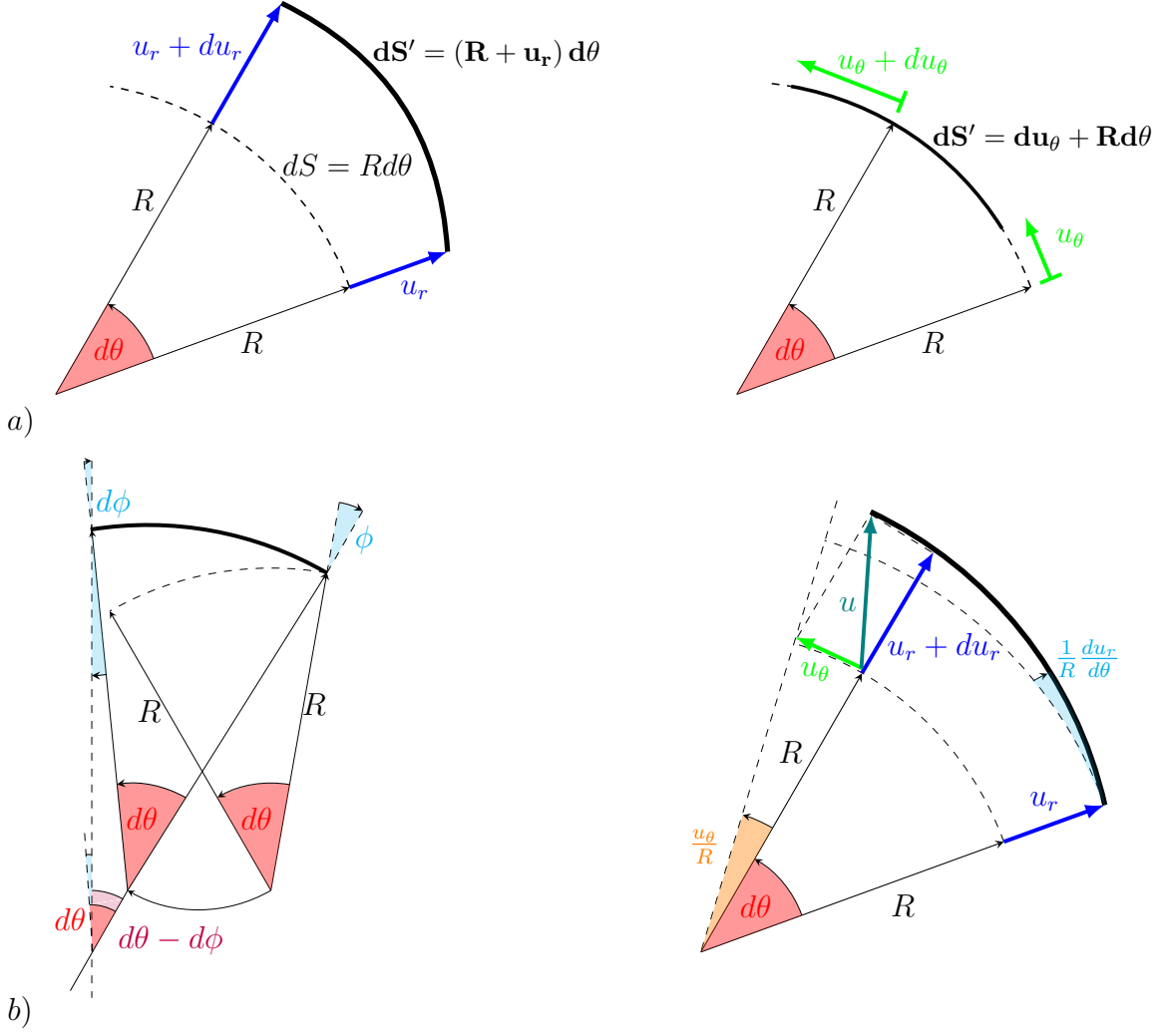


Figure 3: Kinematics of a circular beam modelling the coating of the elastic disk. a) On an infinitesimal beam element the sum of both radial u_r and tangential u_θ displacement generate a total length variation ϵ described by Eq. 2. b) The rotation ϕ of a cross section of the beam is related to $d\theta/d\phi$, the tangential displacement u_θ , and the increment du_r .

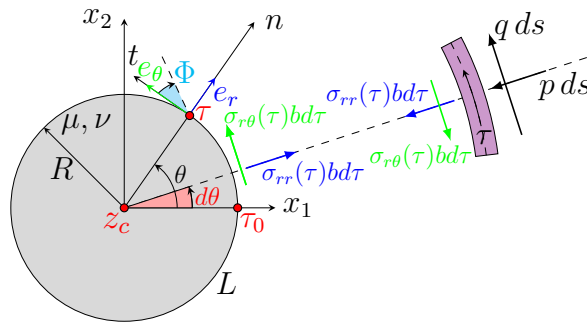


Figure 4: Elastic disk coated with an inextensible and unshearable elastic beam (with bending stiffness EJ).

In the elastic disk, the strain components, expressed in polar coordinates r and θ , are

$$\epsilon_{rr} = u_{r,r}, \quad \epsilon_{\theta\theta} = \frac{u_r + u_{\theta,\theta}}{r}, \quad \epsilon_{r\theta} = \frac{u_{r,\theta} - u_\theta}{2r} + \frac{u_{\theta,r}}{2}, \quad (12)$$

so that, using Hooke's laws, the stress components become

$$\sigma_{rr} = \mu \frac{(1+k)\epsilon_{rr} + (3-k)\epsilon_{\theta\theta}}{k-1}, \quad \sigma_{\theta\theta} = \mu \frac{(1+k)\epsilon_{\theta\theta} + (3-k)\epsilon_{rr}}{k-1}, \quad \sigma_{r\theta} = 2\mu\epsilon_{r\theta}, \quad (13)$$

and vice-versa

$$\epsilon_{rr} = \frac{(1+k)\sigma_{rr} + (k-3)\sigma_{\theta\theta}}{8\mu}, \quad \epsilon_{\theta\theta} = \frac{(1+k)\sigma_{\theta\theta} + (k-3)\sigma_{rr}}{8\mu}, \quad \epsilon_{r\theta} = \frac{\sigma_{r\theta}}{2\mu}, \quad (14)$$

where

$$\kappa = \begin{cases} 3-4\nu, & \text{for plane strain,} \\ \frac{3-\nu}{1+\nu}, & \text{for plane stress.} \end{cases} \quad (15)$$

2.3 Complex potential representation for the disk

The elastic disk of radius R , enclosed by the annular beam defining the coating, has a smooth, non intersecting boundary, so that the tangential and normal directions can be used and respectively denoted by the unit vectors \mathbf{e}_r and \mathbf{e}_θ . Every point of the disk can be identified by a complex number $z = x_1 + ix_2$, so that points belonging to the boundary L will be denoted as $\tau = R e^{i\theta}$. The following notation is introduced

$$g(\tau) = \frac{R}{\tau}, \quad \overline{g(\tau)} = \frac{R}{\bar{\tau}} = g^{-1}(\tau), \quad g'(\tau) = -\frac{1}{R} g^2(\tau), \quad (16)$$

where the prime, $()'$, denotes differentiation with respect to the variable τ , while a superscript bar indicates complex conjugate.

In a complex variable formulation, complex combinations are introduced for displacements, boundary tractions, and external load. These combinations allow the governing equations for the problem (1), (4) and (6) to be rewritten in a way that the elastic fields are determined in terms of complex Fourier series involving unknown complex coefficients. The knowledge of the latter coefficients permits the evaluation of displacements and stresses everywhere in the disk via Kolosov-Muskhelishvili complex potentials $\varphi(z)$ and $\psi(z)$ defined as [49]

$$\begin{cases} 2\mu u(z) = \kappa\varphi(z) - z\overline{\varphi'(z)} - \overline{\psi(z)}, \\ \sigma_{11} + \sigma_{22} = 4\text{Re}(\varphi'(z)), \\ \sigma_{22} - \sigma_{11} + 2i\sigma_{12} = 2[\bar{z}\varphi''(z) + \psi'(z)], \end{cases} \quad (17)$$

where $\text{Re}(\)$, and in the following $\text{Im}(\)$, represent the real and the imaginary part of the enclosed quantity.

The components of the strain tensor can be expressed via the inverse Hooke's law as

$$\begin{cases} \varepsilon_{11} + \varepsilon_{22} = 2\frac{1-2\nu}{\mu}\text{Re}(\varphi'(z)), \\ \varepsilon_{22} - \varepsilon_{11} + 2i\varepsilon_{12} = \frac{1}{\mu}[\bar{z}\varphi''(z) + \psi'(z)]. \end{cases} \quad (18)$$

When dealing with a circular disk, the general expression for the complex potentials $\varphi(z)$ and $\psi(z)$ has been stated by Mogilevskaya et al. [26] as

$$\begin{aligned}\varphi(z) &= \frac{2\mu}{\kappa-1} \operatorname{Re}(A_1) g^{-1}(z) + \frac{2\mu}{\kappa} \sum_{n=1}^{\infty} A_{n+1} g^{-(n+1)}(z), \\ \psi(z) &= -\frac{2\mu}{\kappa-1} \operatorname{Re}(A_1) \frac{\bar{z}_c}{R} - \frac{2\mu}{\kappa} \left[\frac{\bar{z}_c}{R} + g(z) \right] \sum_{n=1}^{\infty} (n+1) A_{n+1} g^{-n}(z) \\ &\quad - 2\mu \sum_{n=2}^{\infty} \overline{A_{1-n}} g^{-(n-1)}(z),\end{aligned}\quad (19)$$

where z_c denotes the centre of the disk and the functions $g(z)$, $g'(z)$, $g''(z)$, and the conjugate $\overline{g(z)}$ are defined as

$$\begin{aligned}g(z) &= \frac{R}{z} = \frac{R}{(x_1 + ix_2)}, \\ g'(z) &= -\frac{1}{R} g^2(z), \\ g''(z) &= \frac{2}{R^2} g^3(z), \\ \overline{g(z)} &= \frac{R^2}{r^2} g^{-1}(z), \\ r &= \sqrt{x_1^2 + x_2^2}.\end{aligned}\quad (20)$$

It will be shown that some of the coefficients A_j ($j = 1, \dots, +\infty$ and $j = -1, \dots, -\infty$) have to be evaluated by imposing additional conditions. In particular, the rigid body motion will be eliminated by fixing points belonging to L . When the latter condition is imposed, the expression for the displacement field in equation (17) becomes

$$u(z) = \frac{1}{2\mu} \left[\kappa \varphi(z) - z \overline{\varphi'(z)} - \overline{\psi(z)} \right] + A_0 + i z \operatorname{Im}(A_1). \quad (21)$$

3 Solution for the coated disk

In a Cartesian coordinate system, the displacement at any point of the boundary of the disk, which coincides with the coating, $\tau \in L$ can be expressed through the complex Fourier series expansion

$$u(\tau) = u_1(\tau) + i u_2(\tau) = \sum_{n=1}^{\infty} A_{-n} g^n(\tau) + \sum_{n=0}^{\infty} A_n g^{-n}(\tau), \quad (22)$$

where $u_1(\tau)$ and $u_2(\tau)$ are displacement components respectively parallel to the x_1 and x_2 axes and the complex coefficients $A_{\pm n}$ are for the moment unknown.

Recalling the relation between Cartesian and polar coordinates,

$$u_r(\tau) + i u_\theta(\tau) = [u_1(\tau) + i u_2(\tau)] g(\tau), \quad (23)$$

it is possible to obtain the displacement at every point τ in the polar coordinate system $(r; \theta)$ as

$$\begin{aligned} u_r(\tau) &= \frac{1}{2} \left[u(\tau) g(\tau) + \overline{u(\tau)} g^{-1}(\tau) \right], \\ u_\theta(\tau) &= \frac{1}{2i} \left[u(\tau) g(\tau) - \overline{u(\tau)} g^{-1}(\tau) \right], \end{aligned} \quad (24)$$

so that the final representation for displacements follows from the equation (22)

$$\begin{aligned} u_r(\tau) &= \frac{1}{2} \left[\sum_{n=1}^{\infty} A_{-n} g^{n+1}(\tau) + \sum_{n=0}^{\infty} A_n g^{-(n-1)}(\tau) + \sum_{n=1}^{\infty} \overline{A_{-n}} g^{-(n+1)}(\tau) + \sum_{n=0}^{\infty} \overline{A_n} g^{n-1}(\tau) \right], \\ u_\theta(\tau) &= \frac{1}{2i} \left[\sum_{n=1}^{\infty} A_{-n} g^{n+1}(\tau) + \sum_{n=0}^{\infty} A_n g^{-(n-1)}(\tau) - \sum_{n=1}^{\infty} \overline{A_{-n}} g^{-(n+1)}(\tau) - \sum_{n=0}^{\infty} \overline{A_n} g^{n-1}(\tau) \right]. \end{aligned} \quad (25)$$

In a similar vein, the tractions at any point of the coating τ can be expressed through the complex Fourier series

$$\sigma(\tau) = \sigma_{rr}(\tau) + i \sigma_{r\theta}(\tau) = \sum_{n=1}^{\infty} B_{-n} g^n(\tau) + \sum_{n=0}^{\infty} B_n g^{-n}(\tau), \quad (26)$$

where σ_{rr} and $\sigma_{r\theta}$ are the components of the traction at the point $\tau \in L$ respectively directed parallel to the normal and the tangential direction.

The coefficients $A_{\pm n}$ and $B_{\pm n}$ are interrelated through the following relations (see Zemlyanova and Mogilevskaya [50])

$$\begin{aligned} B_{-1} &= 0, \\ \frac{\kappa - 1}{2\mu} B_0 &= \frac{2}{R} \operatorname{Re}(A_1), \\ \frac{1}{2\mu} B_{-n} &= \frac{n-1}{R} A_{1-n}, \quad \text{for } n \geq 2, \\ \frac{\kappa}{2\mu} B_n &= \frac{n+1}{R} A_{n+1}, \quad \text{for } n \geq 1. \end{aligned} \quad (27)$$

The representation of the load acting on the external surface of the coating is introduced in its local coordinates system, using the following complex Fourier series as (Fig. 4):

$$p + iq = \sum_{n=1}^{\infty} D_{-n} g^n(\tau) + \sum_{n=0}^{\infty} D_n g^{-n}(\tau), \quad (28)$$

where the components of the load p and q are assumed to be single-valued on L and variable with the angle θ , while coefficients $D_{\pm n}$ remain determined as the series expansion of p and q , so that they are treated as known complex coefficients. The complex representation of the total load affecting the coating, P , equation (11), can be computed by recalling equations (26) and (28) to obtain

$$P(\tau) = \sum_{n=1}^{\infty} (D_{-n} + b \overline{B_n}) g^n(\tau) + \sum_{n=0}^{\infty} (D_n + b \overline{B_{-n}}) g^{-n}(\tau). \quad (29)$$

3.1 Modelling of inextensible coating

The axial strain in the coating, equation (2)₁, can be translated into the complex notation as shown in [50], their equation (99)₂, namely,

$$u_{\theta,\theta}(\tau) + u_r(\tau) = R \operatorname{Re} \left(\frac{\partial u(\tau)}{\partial \tau} \right), \quad (30)$$

so that the inextensibility condition for the annular beam, in other words the isoperimetric constraint, equation (4), becomes

$$\operatorname{Re} \left(\frac{\partial u(\tau)}{\partial \tau} \right) = 0. \quad (31)$$

Differentiating equation (22) with respect to τ and using the resulting g' into equation (16)₃ yields

$$\frac{\partial u(\tau)}{\partial \tau} = \frac{1}{R} \sum_{n=1}^{\infty} (-n A_{-n} g^{n+1}(\tau) + n A_n g^{-(n-1)}(\tau)), \quad (32)$$

so that, a substitution into equation (31) leads to

$$\sum_{n=1}^{\infty} (n A_{-n} g^{n+1}(\tau) - n A_n g^{-(n-1)}(\tau) + n \overline{A_{-n}} g^{-(n+1)}(\tau) - n \overline{A_n} g^{n-1}(\tau)) = 0. \quad (33)$$

By collecting terms with the same power of $g^{\pm n}(z)$ in the left hand side of equation (33) and by equating them to zero leads to the following conditions.

(i.) For $n = 0$:

$$\operatorname{Re}(A_1) = 0, \quad (34)$$

(ii.) For $n = -1$:

$$A_2 = 0, \quad (35)$$

(iii.) For $n \neq 0$ and $n \neq -1$:

$$A_{n+1} = \frac{n-1}{n+1} \overline{A_{1-n}}. \quad (36)$$

Recalling the relation between coefficients A_n and B_n expressed by equations (27), $B_0 = 0$ follows from equation (34). Moreover, setting $n = 1$ in equation (27)₄ and recalling equation (35), $B_1 = 0$ follows.

3.2 Equilibrium and kinematic condition

The 5-th order differential equation (7) describing the radial displacement couples with equilibrium and kinematics of the beam representing the coating, under the constraint of axial inextensibility (4). The perfect bonding between coating and disk, equation (8) implies that the radial displacement entering equation (7) coincides with the radial displacement at the boundary of the disk. In particular, it is possible to rewrite the differential equation (7) through an identification of the components of the external load p and q provided by equation (10). At the right hand side of equation (7), the quantity $(q - dp/d\theta)$ assumes the form

$$q - \frac{dp}{d\theta} = q - p_{,\theta} - b[\sigma_{r\theta}(\tau) + \sigma_{rr,\theta}(\tau)], \quad (37)$$

where the terms on the right hand side can be particularized by exploiting the similarity with equation (98) in [50] as

$$\begin{aligned} \frac{q - p_{,\theta}}{R} &= \text{Im} \left(\frac{\partial}{\partial \tau} [(p + i q) g^{-1}(\tau)] \right), \\ \sigma_{r\theta}(\tau) + \sigma_{rr,\theta}(\tau) &= 2\sigma_{r\theta}(\tau) - R \text{Im} \left(\frac{\partial}{\partial \tau} [\sigma(\tau) g^{-1}(\tau)] \right). \end{aligned} \quad (38)$$

Equation (20)₂ for the derivatives and expressions (26) and (28) lead to

$$\begin{aligned} q - p_{,\theta} &= -\frac{1}{2i} \left\{ \sum_{n=1}^{\infty} [(n-1) D_{-n} + (n+1) \overline{D_n}] g^n(\tau) \right. \\ &\quad \left. - \sum_{n=1}^{\infty} [(n+1) D_n + (n-1) \overline{D_{-n}}] g^{-n}(\tau) \right\} + \text{Im}(D_0), \\ \sigma_{r\theta}(\tau) + \sigma_{rr,\theta}(\tau) &= \frac{1}{2i} \left\{ \sum_{n=1}^{\infty} [(n+1) B_{-n} + (n-1) \overline{B_n}] g^n(\tau) \right. \\ &\quad \left. - \sum_{n=1}^{\infty} [(n-1) B_n + (n+1) \overline{B_{-n}}] g^{-n}(\tau) \right\} + \text{Im}(B_0). \end{aligned} \quad (39)$$

Through a substitution of equations (39), the expression (37) can now be cast in the form

$$\begin{aligned} q - \frac{dp}{d\theta} &= -\frac{1}{2i} \left\{ \sum_{n=1}^{\infty} [(n+1) (\overline{D_n} + b B_{-n}) + (n-1) (D_{-n} + b \overline{B_n})] g^n(\tau) \right. \\ &\quad \left. - \sum_{n=1}^{\infty} [(n+1) (D_n + b \overline{B_{-n}}) + (n-1) (\overline{D_{-n}} + b B_n)] g^{-n}(\tau) \right\} + \text{Im}(D_0 - b B_0). \end{aligned} \quad (40)$$

The left hand side of equation (7) can be written in terms of coefficients $A_{\pm n}$ by computing the complex derivatives of the displacement in equation (24)₂. In particular, the same procedure reported in [50], their Appendix C, yields now

$$\begin{aligned} \frac{d^5 u_r}{d\theta^5} + 2 \frac{d^3 u_r}{d\theta^3} + \frac{du_r}{d\theta} &= -R^5 \text{Im} \left(\frac{\partial^5 u(\tau)}{\partial \tau^5} g^{-4}(\tau) \right) - 5R^4 \text{Im} \left(\frac{\partial^4 u(\tau)}{\partial \tau^4} g^{-3}(\tau) \right) \\ &\quad - 3R^3 \text{Im} \left(\frac{\partial^3 u(\tau)}{\partial \tau^3} g^{-2}(\tau) \right), \end{aligned} \quad (41)$$

where, in agreement with [50] [their equation (100)], the derivatives of the complex rep-

resentation of the displacement field reads as

$$\begin{aligned}\frac{\partial^3 u(\tau)}{\partial \tau^3} &= \frac{1}{R^3} \left[- \sum_{n=1}^{\infty} n(n+1)(n+2) A_{-n} g^{n+3}(\tau) \right. \\ &\quad \left. + \sum_{n=3}^{\infty} n(n-1)(n-2) A_n g^{-(n-3)}(\tau) \right], \\ \frac{\partial^4 u(\tau)}{\partial \tau^4} &= \frac{1}{R^4} \left[+ \sum_{n=1}^{\infty} n(n+1)(n+2)(n+3) A_{-n} g^{n+4}(\tau) \right. \\ &\quad \left. + \sum_{n=4}^{\infty} n(n-1)(n-2)(n-3) A_n g^{-(n-4)}(\tau) \right], \\ \frac{\partial^5 u(\tau)}{\partial \tau^5} &= \frac{1}{R^5} \left[- \sum_{n=1}^{\infty} n(n+1)(n+2)(n+3)(n+4) A_{-n} g^{n+5}(\tau) \right. \\ &\quad \left. + \sum_{n=5}^{\infty} n(n-1)(n-2)(n-3)(n-4) A_n g^{-(n-5)}(\tau) \right].\end{aligned}\quad (42)$$

A complete form of equation (41) can be computed after substitution of expressions (42) as

$$\begin{aligned}\frac{d^5 u_r}{d\theta^5} + 2 \frac{d^3 u_r}{d\theta^3} + \frac{du_r}{d\theta} &= \frac{1}{2i} \left\{ \sum_{n=1}^{\infty} n^2 (n+1)(n+2)^2 [A_{-n} g^{n+1}(\tau) - \overline{A_{-n}} g^{-(n+1)}(\tau)] \right. \\ &\quad \left. - \sum_{n=3}^{\infty} n^2 (n-1)(n-2)^2 [A_n g^{-(n-1)}(\tau) - \overline{A_n} g^{n-1}(\tau)] \right\}.\end{aligned}\quad (43)$$

Using expressions (40) and (43) and collecting terms with the same summation index, the differential equation (7) becomes

$$\begin{aligned}& - \sum_{n=1}^{\infty} \frac{R^4}{EJ} \{ [(n+1)(\overline{D_n} + b B_{-n}) + (n-1)(D_{-n} + b \overline{B_n})] g^n(\tau) \\ & - [(n+1)(D_n + b \overline{B_{-n}}) + (n-1)(\overline{D_{-n}} + b B_n)] g^{-n}(\tau) - 2i \operatorname{Im}(D_0 - b B_0) \} \\ & - n^2 (n+1)(n+2)^2 [A_{-n} g^{n+1}(\tau) - \overline{A_{-n}} g^{-(n+1)}(\tau)] \\ & + \sum_{n=3}^{\infty} n^2 (n-1)(n-2)^2 [A_n g^{-(n-1)}(\tau) - \overline{A_n} g^{n-1}(\tau)] = 0,\end{aligned}\quad (44)$$

from which, collecting terms with the same power $g^{\pm n}(\tau)$ in equation (44) and equating them to zero, the following expression is obtained

$$\begin{aligned}& (n+1)(\overline{D_n} + b B_{-n}) + (n-1)(D_{-n} + b \overline{B_n}) \\ & + \frac{n(n+1)^2 (n-1)^2 EJ}{R^4} [A_{1-n} + \overline{A_{n+1}}] = 0,\end{aligned}\quad (45)$$

of which the following two particular cases can be highlighted

$$\operatorname{Im}(D_0 - bB_0) = 0, \quad \text{for } n = 0 \quad \text{and} \quad \overline{B_{-1}} = -\frac{1}{b}D_1, \quad \text{for } n = -1. \quad (46)$$

Recalling equations (27)₃₋₄ and (36), it becomes possible to express the coefficients $B_{\pm n}$ involved in equation (45) as functions of the coefficients $A_{\pm n}$

$$\begin{aligned} \overline{B_n} &= \frac{2\mu}{\kappa R} (n+1) \overline{A_{n+1}} = \frac{2\mu}{\kappa R} (n-1) A_{1-n}, \quad \text{for } n \geq 1 \\ B_{-n} &= \frac{2\mu}{R} (n-1) A_{1-n}, \quad \text{for } n \geq 2. \end{aligned} \quad (47)$$

A substitution of equations (47) into equation (45) yields

$$\begin{aligned} (n+1) \overline{D_n} + \frac{2\mu b}{R} (n^2 - 1) A_{1-n} + (n-1) D_{-n} + \frac{2\mu b}{\kappa R} (n-1)^2 A_{1-n} \\ + \frac{2n^2 (n+1) (n-1)^2 EJ}{R^4} A_{1-n} = 0, \end{aligned} \quad (48)$$

so that collecting terms involving A_{1-n} leads to

$$A_{1-n} = -\frac{\kappa R^4 [(n+1) \overline{D_n} + (n-1) D_{-n}]}{2(n-1) [\kappa EJ n^2 (n^2 - 1) + R^3 \mu b (n + \kappa n + \kappa - 1)]}, \quad \text{for } n \geq 2. \quad (49)$$

3.3 Fixing rigid body motion

Equation (21) shows that restrictions on coefficients A_0 and A_1 can be inferred from the imposition of a rigid-body roto-translation. Following the procedure adopted in [26], the latter will be eliminated by assuming the displacement of the disk to be zero at one point of it and requiring vanishing of the vertical displacement component at another point of the disk on the same horizontal line. It will now be imposed $u(z) = 0$ at points $z = \tau_0 = R + i0$ and $z = z_c = 0$, see Fig. (4) a. Recalling equations (34)-(36) and setting $z_c = 0$ in relations (19), the complex potentials for the disk are determined as

$$\begin{aligned} \varphi(z) &= \frac{2\mu}{\kappa} \sum_{n=1}^{\infty} A_{n+1} g^{-(n+1)}(z), \\ \psi(z) &= -2\mu \sum_{n=2}^{\infty} \left(\frac{n + \kappa - 1}{\kappa} \right) \overline{A_{1-n}} g^{-(n-1)}(z). \end{aligned} \quad (50)$$

At points $z = z_c$ and $z = \tau_0$ the following results can be derived from equations (21).

- At $z = z_c$:

$$u(z_c) = \frac{1}{2\mu} [\kappa \varphi(z_c) - \overline{\psi(z_c)}] + A_0, \quad (51)$$

so that equations (20)₁₋₂, (34) and (35) lead to the particularization of equation (50) at $z = z_c$

$$\varphi(z_c) = \psi(z_c) = 0, \quad (52)$$

in addition to which equations (52), substituted into equation (51) with $u(z_c) = 0$, provide $A_0 = 0$.

- At $z = \tau_0$:

$$u(\tau_0) = \frac{1}{2\mu} \left[\kappa \varphi(\tau_0) - \tau_0 \overline{\varphi'(\tau_0)} - \overline{\psi(\tau_0)} \right] + i \tau_0 \operatorname{Im}(A_1), \quad (53)$$

from which the following specific expressions for the complex potentials (50) can be derived

$$\varphi(\tau_0) = \frac{2\mu}{\kappa} \sum_{n=1}^{\infty} A_{n+1}, \quad (54)$$

$$\varphi'(\tau_0) = \frac{2\mu}{R\kappa} \sum_{n=1}^{\infty} (n+1) A_{n+1},$$

and

$$\psi(\tau_0) = -2\mu \sum_{n=2}^{\infty} \left(\frac{n+\kappa-1}{\kappa} \right) \overline{A_{1-n}}, \quad (55)$$

where the latter expressions have been obtained by setting $\tau_0 = R$ in equations (16), i.e. $g(\tau_0)^{-n} = (\tau_0/R)^n = 1 \forall n \geq 0$. An explicit expression for $u(\tau_0)$ can be obtained through a substitution of equations (54) and (55) into equation (53)

$$u(\tau_0) = \sum_{n=1}^{\infty} A_{n+1} - \frac{1}{\kappa} \sum_{n=1}^{\infty} (n+1) \overline{A_{n+1}} + \sum_{n=2}^{\infty} \left(\frac{n+\kappa-1}{\kappa} \right) A_{1-n} + iR \operatorname{Im}(A_1), \quad (56)$$

which, recalling equations (35) and (36), provides

$$u(\tau_0) = \sum_{n=2}^{\infty} \left[\frac{n-1}{n+1} \overline{A_{1-n}} + A_{1-n} \right] + iR \operatorname{Im}(A_1). \quad (57)$$

Imposition of the condition $u_2(\tau_0) = \operatorname{Im}(u(\tau_0))$ in equation (57) yields

$$u_2(\tau_0) = \operatorname{Im} \left(\sum_{n=2}^{\infty} \left[\frac{n-1}{n+1} \overline{A_{1-n}} + A_{1-n} \right] \right) + R \operatorname{Im}(A_1). \quad (58)$$

The requirement that the vertical displacement component $u_2(\tau_0)$ be zero at $z = \tau_0$ is finally established from the vanishing of the right hand side of equation (58),

$$\operatorname{Im}(A_1) = -\frac{2}{R} \operatorname{Im} \left(\sum_{n=2}^{\infty} \frac{1}{n+1} A_{1-n} \right). \quad (59)$$

The condition $A_0 = 0$ at $z = z_c$ and equation (59) allow to derive all additional terms in equation (21), describing a rigid body movement.

The above obtained solution is summarized in terms of the evaluated coefficients reported in Tables 1 and 2. These coefficients completely define the displacement and stress fields for the coated disk.

Coefficient	Value	Rule
A_{1-n}	$-\frac{\kappa R^4 [(n+1)\overline{D_n} + (n-1)D_{-n}]}{2(n-1)[\kappa E J n^2 (n^2-1) + R^3 \mu b (n + \kappa n + \kappa - 1)]}$	$n \geq 2$
$A_0 = A_2$	0	-
A_1	$-\frac{2i}{R} \text{Im} \left(\sum_{n=2}^{\infty} \frac{1}{n+1} A_{1-n} \right)$	-
A_{n+1}	$\frac{n-1}{n+1} \overline{A_{1-n}}$	$n > 1$

Table 1: Coefficients $A_{\pm n}$ of the complex power series defining the displacement field within the disk.

Coefficients $A_{\pm n}$ listed in Table 1 are given in terms of the known complex coefficients $D_{\pm n}$, which define the loads applied to the external surface of the coated disk.

Coefficient	Value	Rule
B_{-n}	$\frac{2\mu}{R} (n-1) A_{1-n}$	$k \geq 2$
$B_{-1} = B_0 = B_1$	0	-
B_n	$\frac{2\mu}{\kappa R} (n-1) \overline{A_{1-n}}$	$k \geq 1$

Table 2: Coefficients $B_{\pm n}$ of the complex power series defining the stress distribution inside the disk.

Table 2 shows that all coefficients $B_{\pm n}$ can be written in terms of coefficients A_{1-n} and hence from equation (49) they are found to depend on the known complex coefficients $D_{\pm n}$. Once $A_{\pm n}$ and $B_{\pm n}$ are known, it becomes possible to compute the expressions for elastic displacement and stress fields.

3.4 Elastic fields for the disk

Displacement, stress, and strain at any point inside the disk and on its boundary are known in terms of complex potentials $\varphi(z)$ and $\psi(z)$, equations (17), through coefficients $A_{\pm n}$ listed in Table 1, as

$$\begin{aligned}\varphi(z) &= \frac{2\mu}{\kappa} \sum_{n=1}^{\infty} \frac{n-1}{n+1} \overline{A_{1-n}} g^{-(n+1)}(z), \\ \varphi'(z) &= \frac{2\mu}{R\kappa} \sum_{n=1}^{\infty} (n-1) \overline{A_{1-n}} g^{-n}(z),\end{aligned}\tag{60}$$

$$\begin{aligned}\varphi''(z) &= \frac{2\mu}{R^2\kappa} \sum_{n=1}^{\infty} n(n-1) \overline{A_{1-n}} g^{-n+1}(z), \\ \psi(z) &= -2\mu \sum_{n=2}^{\infty} \left(\frac{n+\kappa-1}{\kappa} \right) \overline{A_{1-n}} g^{-n+1}(z), \\ \psi'(z) &= -\frac{2\mu}{R} \sum_{n=2}^{\infty} (n-1) \left(\frac{n+\kappa-1}{\kappa} \right) \overline{A_{1-n}} g^{-n+2}(z).\end{aligned}\tag{61}$$

Except for a rigid roto-translation, the displacement $u(z)$ at every point of the disk is determined by relation (17)₁, through equation (21) and the coefficients listed in Tables 1 and 2 entering the following equation

$$u(z) = \sum_{n=1}^{\infty} A_{n+1} g^{-n-1}(z) + \sum_{n=2}^{\infty} A_{1-n} g^{n-1}(z) - 2i g^{-1}(z) \operatorname{Im} \left(\sum_{n=2}^{\infty} \frac{1}{n+1} A_{1-n} \right), \quad (62)$$

which, recalling equations (35) and (36) and collecting terms, can be rewritten as

$$u(z) = \sum_{n=2}^{\infty} \left[\frac{n-1}{n+1} \overline{A_{1-n}} g^{-(n+1)}(z) + A_{1-n} g^{n-1}(z) - 2i g^{-1}(z) \operatorname{Im} \left(\frac{1}{n+1} A_{1-n} \right) \right]. \quad (63)$$

The stress is determined from a combination between equations (17)₂₋₃, with a chain substitution of equations (35) and (36) into the potentials, equations (50)₁, as

$$\sigma_{11} + \sigma_{22} = \frac{8\mu}{R\kappa} \operatorname{Re} \left(\sum_{n=2}^{\infty} (n-1) \overline{A_{1-n}} g^{-n}(z) \right), \quad (64)$$

while equation (17)₃ leads to

$$\sigma_{22} - \sigma_{11} + 2i\sigma_{12} = \frac{4\mu}{R} \sum_{n=2}^{\infty} (n-1) \left[\frac{r^2}{R^2\kappa} n - \frac{1}{\kappa} (n-1) - 1 \right] \overline{A_{1-n}} g^{-n+2}(z). \quad (65)$$

4 Experiments vs. theoretical predictions

The aim of this section is to introduce the experimental set-up and results and compare the latter with the general solution for the coated disk, to be particularized now to a specific applied loading, tailored to model the experiments.

4.1 Photoelastic experiments

The previously derived analytic solution is compared with photoelastic experiments performed at the Instabilities Lab of the University of Trento on two coated disks, subject to two radial compressive force distributions applied at two diametrically opposed small portions of the coating. The two coated disks, shown in Fig. 5 on the left, have been machined with radii R_1 and R_2 equal to 60 and 35 mm and thickness 5 mm in the internal portion (with a CNC engraving machine) from a single thick plate of polymethyl methacrylate (Perspex Clear, Lucite International, Young modulus $E = 3200$ MPa and Poisson's ratio $\nu = 0.36$). The coatings have in-plane \times out-of-plane thicknesses equal to 14 mm \times 19 mm and 5 mm \times 21 mm, respectively.

The fact that the coated disks have been obtained by carving a single block of material implies that the bonding between disk and coating is perfect and that the sample is obtained without introducing any residual stress, so that detachments are excluded until failure. Note that failure cannot be investigated with the proposed experimental set-up, because it involves out-of-plane buckling and may break the polariscope.

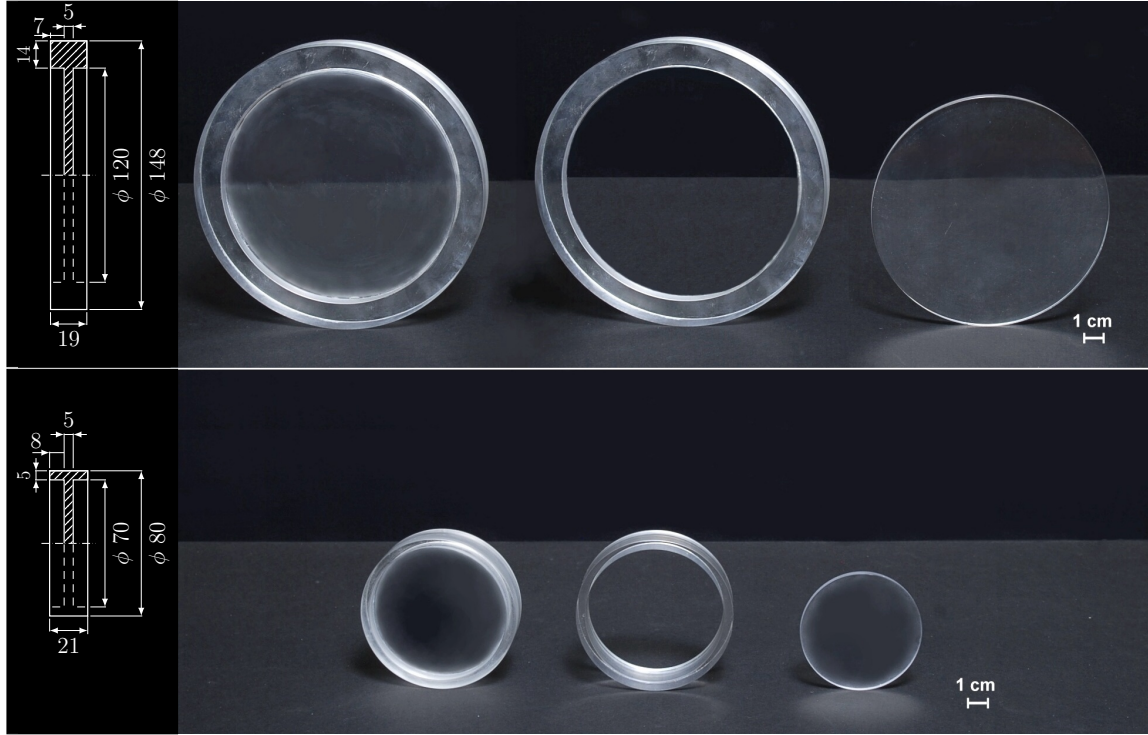


Figure 5: The two families of samples used for diametrical compression tests: the coated disk (left), the coating alone, representing a circular beam (center) and disk without coating (right). The coating has a rectangular cross-section equal to 14×19 mm (upper part) and 5×21 mm (lower part), resulting in a strongly different bending stiffness for the coating, when the two families of samples are compared.

For comparison, both the interior disk and the external coating of the coating/disk complex have also been machined into separate pieces, shown in Fig. 5 on the center and on the right. In this way, the inner disk, the annular beam representing the coating, and the coated disk have all been individually tested.

Vertical load has been quasi-statically increased through compression against two horizontal steel plates, equipped with a loading cell (TH-KN2D load cell RC 20 kN, from Gefran) to measure (signal was acquired with a NI CRio interfaced via software Labview, ver. 2018 from National Instruments) the applied load, under displacement control (imposed through an electromechanical testing machine, ELE Tritest 50, by ELE International Ltd). The samples under loading have been analyzed with a linear and circular polariscope (with quarterwave retarders for 560nm, dark field arrangement; equipped with a white and sodium vapor lightbox at $\lambda = 589.3\text{nm}$, purchased from Tiedemann & Betz), designed and manufactured at the Instabilities Lab of the University of Trento.

Photos at white and monochromatic light were taken with a Nikon D200 digital camera, equipped with a AF-S micro Nikkor (105 mm, 1:2.8G ED) or with a AF-S micro Nikkor (70180 mm, 1:4.55.6 D) lens. Monitored with a thermocouple connected to a Xplorer GLX Pasco[®], temperature near the samples during experiments was found to lie around 22.5°C , without sensible oscillations.

4.1.1 Analysis of the experimental results

Photos taken during the tests at increasing values of loading are reported in Fig. 6 at monochromatic light, and in Fig. 7 at white light (for the coated disk samples reported in Fig. 5).

Starting the discussion with Fig. 6 (referred to the samples visible in Fig. 5, upper part), it should be noted that the loads for the three samples are different, higher for the coated disk (on the left, 10 kN), low for the ring (central part, 0.6 kN), and intermediate for the uncoated disk (on the right 4.6 kN). This choice has been guided by the fact that at the value used for the coated disk the ring would break and the uncoated disk would suffer an out-of-plane buckling, while at the value used for the ring the coated disk is loaded so little that the fringes are barely visible.

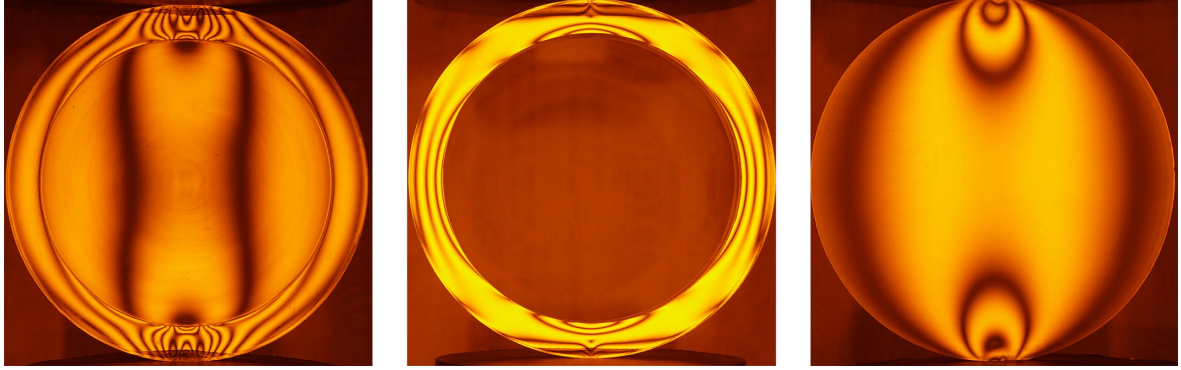


Figure 6: Monochromatic photoelastic fringes under diametrical compression of: a coated disk (left), its external ring (center), and the inner disk without coating (right). Samples are shown in Fig. 5 (upper part).

Experiments on the uncoated disk are well-known [51], so that only one additional is reported in Appendix A, used to calibrate the other photoelastic analyses.

Further experimental results on the ring, together with comparisons with the calculated stress state, are deferred to Appendix B. These photoelastic analyses show that the ring behaves as a circular Euler-Bernoulli beam, where flexural deformation prevails. Therefore, the coating can be modelled with excellent approximation as inextensible, because the ratio between flexural and axial stiffnesses becomes negligible. To substantiate this statement with an evaluation, an annular beam of radius R is assumed to be both flexurally and axially deformable and subject to two diametrical forces F . The shortening of the diameter of the rod can be written as

$$\Delta = \frac{(\pi^2 - 8) R^3}{4\pi EJ} \left[1 + \underbrace{\frac{\pi^2}{\pi^2 - 8} \left(\frac{\rho}{R} \right)^2}_{\text{axial deformability}} \right], \quad (66)$$

where ρ is the radius of inertia of the cross section of the beam. Considering the data pertaining to our experiments, Fig. 5, effects related to the axial deformability of the coating can be evaluated as 0.024 and 0.009, to be compared with 1, representing the flexural deformability.

The fringe pattern reported in Fig. 6 evidences the deep effect connected to the presence of the coating, which introduces a nonlocal distribution of the external load, thus strongly affecting the stress state in the disk.

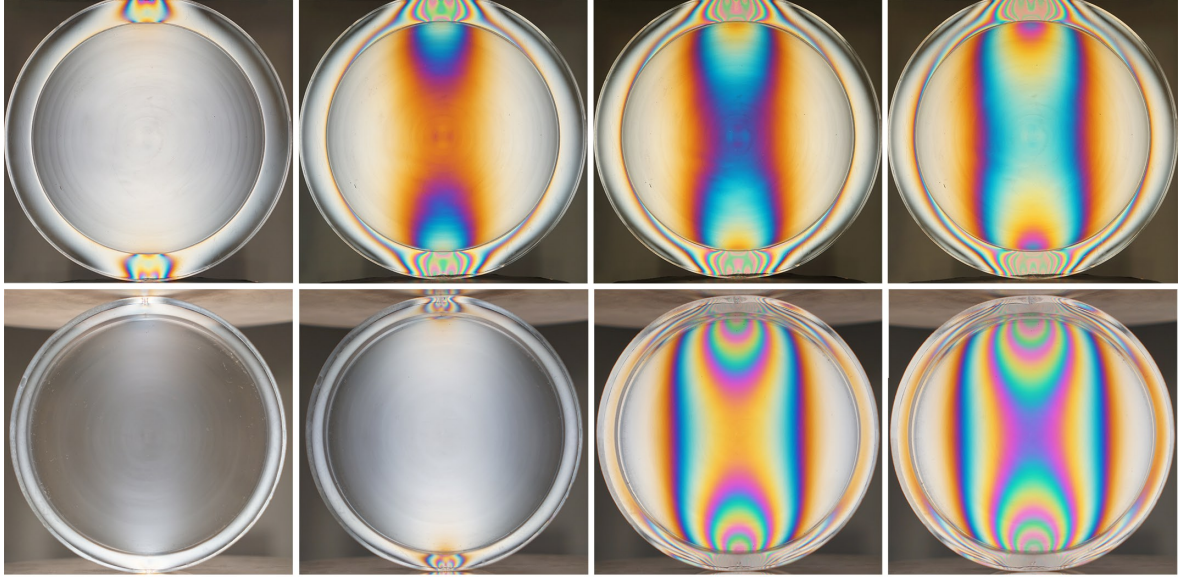


Figure 7: Photoelastic fringes generated during (vertical) diametrical compression in the coated disks with bending stiffness of the coating $EJ_1=1.4 \cdot 10^{-2} \text{ kNm}^2$ (upper part) and $EJ_2=7 \cdot 10^{-4} \text{ kNm}^2$ (lower part). Four increasing values of compression are reported: 3.0 kN (1 kN), 7.0 kN (2.5 kN), 8.5 kN (7.0 kN), and 10.0 kN (8.5 kN) in the upper part (lower part), for the samples shown in Fig. 5; photos have been taken at white circularly polarized light.

Considering now Fig. 7 the photographs refer to four different values of loading, namely, 3.0 kN (1 kN), 7.0 kN (2.5 kN), 8.5 kN (7.0 kN), and 10.0 kN (8.5 kN) in the upper part (in the lower part).

Although the stress states for the two experiments reported in the figure are qualitatively similar, it is clear that the effect of coating is strongly increased in the case of thick coating (upper part of the figure). The fringes visualized in the above reported photoelastic experiments provide a measure of the difference between the in plane principal stresses (for more details see [51])

$$|\sigma_I - \sigma_{II}| = \sqrt{(\sigma_{11} - \sigma_{22})^2 + 4\sigma_{12}^2}, \quad (67)$$

thus permitting a comparison with the analytical solution derived in the previous Sections, that will be applied to a loading distribution modelling the load during the experiments and considered in the following Sections. The comparison, anticipated in Fig. 1, shows that the analytical solution excellently models the experimental results.

4.2 An analytical solution for the coated disk modelling the experiments

In order to apply the general solution for the coated disk obtained in Section 3, the traction distribution acting on the external portion of the coating has to be modelled and implemented. These are the subjects of the present section.

4.2.1 Model for the external load applied on the coated disk

The external load will be modelled as a constant normal traction p ($q = 0$) applied along two diametrically opposed small arcs of equal amplitude, $s = \alpha R$, where α is an angle centred at the vertical diameter of the disk. Using the complex Fourier series expansion (28), multiplying both sides of it by $e^{-mi\theta}$, $m = \pm 1, \pm 2, \dots \pm n$ and integrating over the whole circle leads to

$$\int_{\frac{\pi}{2}-\alpha}^{\frac{\pi}{2}+\alpha} p e^{-mi\theta} d\theta + \int_{\frac{3\pi}{2}-\alpha}^{\frac{3\pi}{2}+\alpha} p e^{-mi\theta} d\theta = \int_0^{2\pi} \left[\sum_{n=1}^{\infty} D_{-n} e^{-(n+m)i\theta} + \sum_{n=0}^{\infty} D_n e^{-(n-m)i\theta} \right] d\theta. \quad (68)$$

The right hand side of equation (68) is different from zero and equal to 2π if and only if $n = m$. Hence, at every fixed m , one non-null coefficient is determined. Collecting terms with the same power of $e^{\pm ni\theta}$ and inverting equation (68) yield the values of all coefficients $D_{\pm n}$.

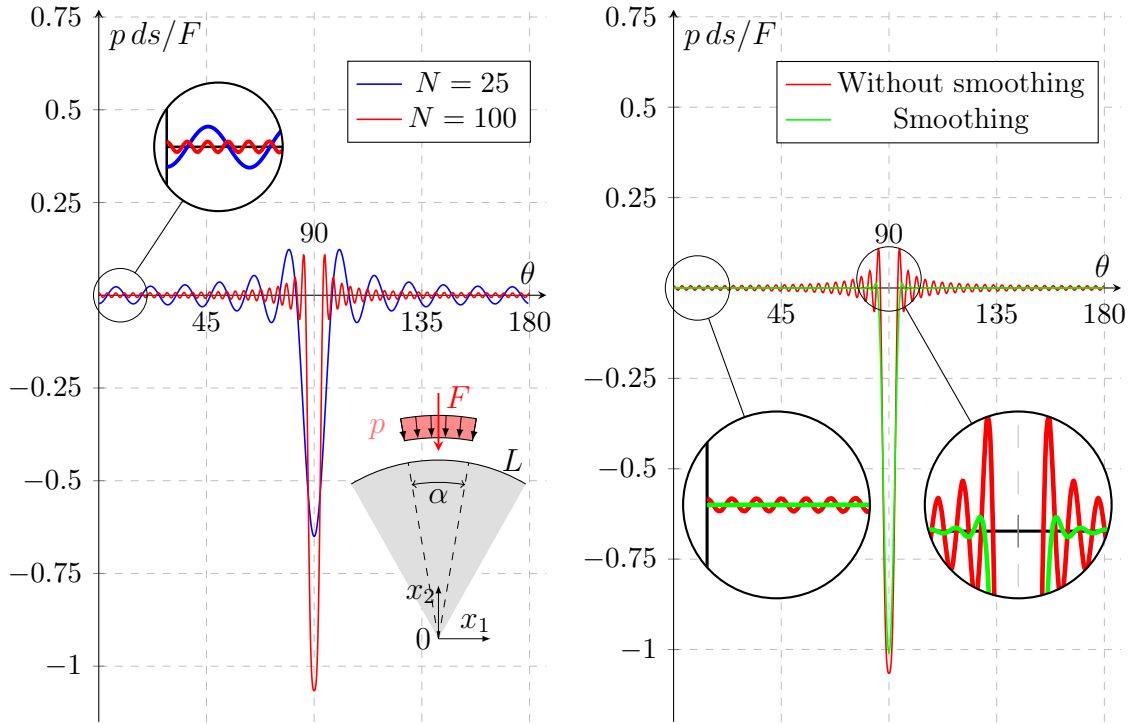


Figure 8: Convergence of the series approximation for the applied load, equation (28), using $N = 25$ and $N = 100$ complex coefficients $D_{\pm n}$ (left). Severe oscillations are evident, as related to the presence of a discontinuity in the applied loads, which should vanishes at $\theta = \pi/2 \mp \alpha$ and $\theta = 3\pi/2 \pm \alpha$. Both global and local oscillation can be filtered out by means of a smoothing technique (right) resulting in a better approximation for the applied external load using $N = 100$ complex coefficients $D_{\pm n}^*$ having the form of equation (75)

The convergence of the series approximation for an applied load of unit resultant is analyzed in Fig. 8 (central part). A satisfactory representation for the applied concentrated load can be obtained with an arc length $\alpha = 5^\circ$ and a truncation of the complex Fourier series at $N = 100$. The convergence of the series is analyzed in Fig. 8 (on the left), where results are reported for $N = 25$ and $N = 100$. Here it may be concluded

that: (i.) the maximum load does not exceed the unit value up to $N = 100$ (for $N = 25$ the maximum value is ≈ 0.65) and (ii.) severe sign variations of the represented function are visible, a phenomenon known as ‘Gibbs oscillations’.

Although the approximation obtained with $N = 100$ is judged as satisfactory and will be used in the following, the local smoothing technique proposed by Lanczos (1966) has been also implemented to further increase the precision in the representation. The Lanczos technique can be explained with reference to a given a Fourier series representation of a function $f(\theta)$, which displays a jump discontinuity, with partial sum

$$f_N(\theta) = a_0 + \sum_{n=1}^N a_n \cos(n\theta) + \sum_{n=1}^N b_n \sin(n\theta). \quad (69)$$

Lanczos (1966) introduced the smoothed value for the partial sum (69) as

$$f_N^*(\theta) = a_0^* + \sum_{n=1}^N \frac{\sin(n\pi/N)}{n\pi/N} [a_n^* \cos(n\theta) + b_n^* \sin(n\theta)]. \quad (70)$$

Using now the complex notation,

$$\cos n\theta = \frac{1}{2} (e^{in\theta} + e^{-in\theta}), \quad \sin n\theta = \frac{1}{2i} (e^{in\theta} - e^{-in\theta}), \quad (71)$$

the partial sum expressed by equation (70) can be rewritten as

$$f_N^*(\theta) = a_0^* + \sum_{n=1}^N \frac{\sin(n\pi/N)}{n\pi/N} \left[\frac{a_n^*}{2} (e^{in\theta} + e^{-in\theta}) + \frac{b_n^*}{2i} (e^{in\theta} - e^{-in\theta}) \right], \quad (72)$$

so that by collecting terms yields

$$f_N^*(\theta) = a_0^* + \sum_{n=1}^N \frac{\sin(n\pi/N)}{n\pi/N} \left[\left(\frac{a_n^* - i b_n^*}{2} \right) e^{in\theta} + \left(\frac{a_n^* + i b_n^*}{2} \right) e^{-in\theta} \right], \quad (73)$$

and adopting the notation used in equation (16) finally leads to

$$f_N^*(\theta) = a_0^* + \sum_{n=1}^N \frac{\sin(n\pi/N)}{n\pi/N} \left[\left(\frac{a_n^* - i b_n^*}{2} \right) g^{-n}(\tau) + \left(\frac{a_n^* + i b_n^*}{2} \right) g^n(\tau) \right]. \quad (74)$$

Equations (74) and (68) allow the determination of the new coefficients D_n^* for the smoothed function

$$\begin{cases} D_0^* = a_0^*, \\ D_{-n}^* = \left(\frac{a_n^* + i b_n^*}{2} \right) \frac{\sin(n\pi/N)}{n\pi/N}, \\ D_n^* = \left(\frac{a_n^* - i b_n^*}{2} \right) \frac{\sin(n\pi/N)}{n\pi/N}, \end{cases} \quad (75)$$

providing a sufficiently accurate representation of the applied load, for appropriate choice of N , as shown in Fig. 8 on the right.

4.2.2 Solution for the coated disk subject to opposite force distributions

All ingredients are now ready to obtain the solution of a coated disk subjected to two equal and opposite distributions of surface tractions of the type shown in Fig. 8. This solution is derived below and will be used for comparison with the experimental results.

A substitution of equations (36) and (49) into equation (50), provides the complex potentials for the coated disk when subjected to two opposite radial traction distributions, written in terms of the coefficients $D_{\pm n}$

$$\begin{aligned}\varphi(z) &= -\mu R^4 \sum_{n=2}^{\infty} \left\{ \frac{(n-1) \overline{D_{-n}} + (n+1) D_n}{(n+1) [\kappa E J n^2 (n^2 - 1) + R^3 \mu b (n + \kappa n + \kappa - 1)]} \right\} g^{-(n+1)}(z), \\ \psi(z) &= \mu R^4 \sum_{n=2}^{\infty} \left\{ \frac{(n-1+\kappa) [(n-1) \overline{D_{-n}} + (n+1) D_n]}{(n-1) [\kappa E J n^2 (n^2 - 1) + R^3 \mu b (n + \kappa n + \kappa - 1)]} \right\} g^{-(n-1)}(z),\end{aligned}\quad (76)$$

so that the displacement follows as

$$\begin{aligned}u(z) &= -\frac{R^4 \kappa}{2} \sum_{n=2}^{\infty} \left\{ \frac{[(n-1) \overline{D_{-n}} + (n+1) D_n]}{(n+1) [\kappa E J n^2 (n^2 - 1) + R^3 \mu b (n + \kappa n + \kappa - 1)]} g^{-(n+1)}(z) \right. \\ &\quad \left. - \frac{[(n-1) D_{-n} + (n+1) \overline{D_n}] [r^2 (n-1) - R^2 (n-1+\kappa)] R^{-2n}}{\kappa (n-1) [\kappa E J n^2 (n^2 - 1) + R^3 \mu b (n + \kappa n + \kappa - 1)] r^{-2(n-1)}} g^{n-1}(z) \right\},\end{aligned}\quad (77)$$

and the stress components, equation (17)₂, as

$$\frac{\sigma_{11} + \sigma_{22}}{4\mu R^3} = -\sum_{n=2}^{\infty} \operatorname{Re} \left(\frac{[(n-1) \overline{D_{-n}} + (n+1) D_n]}{\kappa E J n^2 (n^2 - 1) + R^3 \mu b (n + \kappa n + \kappa - 1)} g^{-n}(z) \right), \quad (78)$$

while, from equation (17)₃, as

$$\frac{\sigma_{22} - \sigma_{11} + 2i\sigma_{12}}{2\mu R} = \sum_{n=2}^{\infty} \frac{[(n-1) \overline{D_{-n}} + (n+1) D_n] [R^2 (n + \kappa - 1) - r^2 n]}{\kappa E J n^2 (n^2 - 1) + R^3 \mu b (n + \kappa n + \kappa - 1)} g^{-(n-2)}(z). \quad (79)$$

The in-plane deviatoric stress can be calculated using equation (67) from the knowledge of σ_{11} , σ_{22} , and σ_{12} .

The results are reported in Fig. 1, where they are compared with the photoelastic experiments performed on the coated disks, shown in Fig. 5. The internal forces in the coating, equations (6), are completely determined by the displacement component u_r in terms of the coefficients A_{1-n} in equation (49). Recalling equations (35) and (36), the derivatives of complex displacement involved in equation (6) are found as

$$\begin{aligned}\frac{du_r}{ds} &= -\frac{1}{R} \sum_{n=1}^{\infty} \operatorname{Im} \left(-(n+1) A_{-n} g^{n+1}(\tau) + (n-1) A_n g^{-(n-1)}(\tau) \right), \\ \frac{d^2 u_r}{ds^2} &= -\frac{1}{R^2} \sum_{n=1}^{\infty} \operatorname{Re} \left((n+1)^2 A_{-n} g^{n+1}(\tau) + (n-1)^2 A_n g^{-(n-1)}(\tau) \right), \\ \frac{d^3 u_r}{ds^3} &= \frac{1}{R^3} \sum_{n=1}^{\infty} \operatorname{Im} \left(-(n+1)^3 A_{-n} g^{n+1}(\tau) + (n-1)^3 A_n g^{-(n-1)}(\tau) \right), \\ \frac{d^4 u_r}{ds^4} &= \frac{1}{R^4} \sum_{n=1}^{\infty} \operatorname{Re} \left((n+1)^4 A_{-n} g^{n+1}(\tau) + (n-1)^4 A_n g^{-(n-1)}(\tau) \right).\end{aligned}\quad (80)$$

A substitution of equations (80) into expressions (6) leads to the internal forces along the coating as

$$\begin{aligned}
 M &= -\frac{EJ}{R^2} \sum_{n=1}^{\infty} n \operatorname{Re}((n+2) A_{-n} g^{n+1}(\tau) + (n-2) A_n g^{-(n-1)}(\tau)), \\
 T &= -\frac{EJ}{R^3} \sum_{n=1}^{\infty} n \operatorname{Im}(-(n+1)(n+2) A_{-n} g^{n+1}(\tau) + (n-1)(n-2) A_n g^{-(n-1)}(\tau)), \\
 N &= -\frac{EJ}{R^3} \sum_{n=1}^{\infty} n \operatorname{Re}((n+2)(n+1)^2 A_{-n} g^{n+1}(\tau) + (n-2)(n-1)^2 A_n g^{-(n-1)}(\tau)) \\
 &\quad - R \operatorname{Re} \left(\sum_{n=1}^{\infty} \left[D_{-n} + \frac{2\mu b}{\kappa R} (n-1) A_{1-n} \right] g^n(\tau) + \sum_{n=0}^{\infty} \left[D_n + \frac{2\mu b}{R} (n-1) \overline{A_{1-n}} \right] g^{-n}(\tau) \right). \tag{81}
 \end{aligned}$$

The two coatings of the disks used in the experiments are characterized by two strongly different bending stiffnesses, namely, $EJ_1 = 1.4 \cdot 10^{-2} \text{ kNm}^2$ and $EJ_2 = 7 \cdot 10^{-4} \text{ kNm}^2$. Analytical results referred to these two rings, coating a disk, are reported in Fig. 9 (only a quarter of the coating is shown) and discriminated with the indices 1 and 2, referring to EJ_1 and EJ_2 , respectively. Normal, N , and shear, T , forces and bending moments, M are reported in panels (a), (b), and (c), as calculated from equations (81). The displacement of the coating u , equation (77), is reported in Panel (d).

Fig. 9 shows that the internal forces and the displacement are quantitatively, but not qualitatively, affected by the stiffness of the coating. The displacement of the coating evidences that a stiff coating leads to a higher non-locality effect.

From the knowledge of the internal forces, N , T , and M , the state of stress at every point of the cross section of the coating can be obtained by considering the model of an annular beam [48]. From the stress distribution, the in-plane deviatoric stress $\sigma_I - \sigma_{II}$ in the coating can be obtained, as reported inside the coatings visible in Figs. 1 and 10.

Additional deviatoric stress distributions, determined inside the annular beams so far considered, but taken as isolated, are reported in Appendix B, where they are compared to the results from photoelastic experiments.

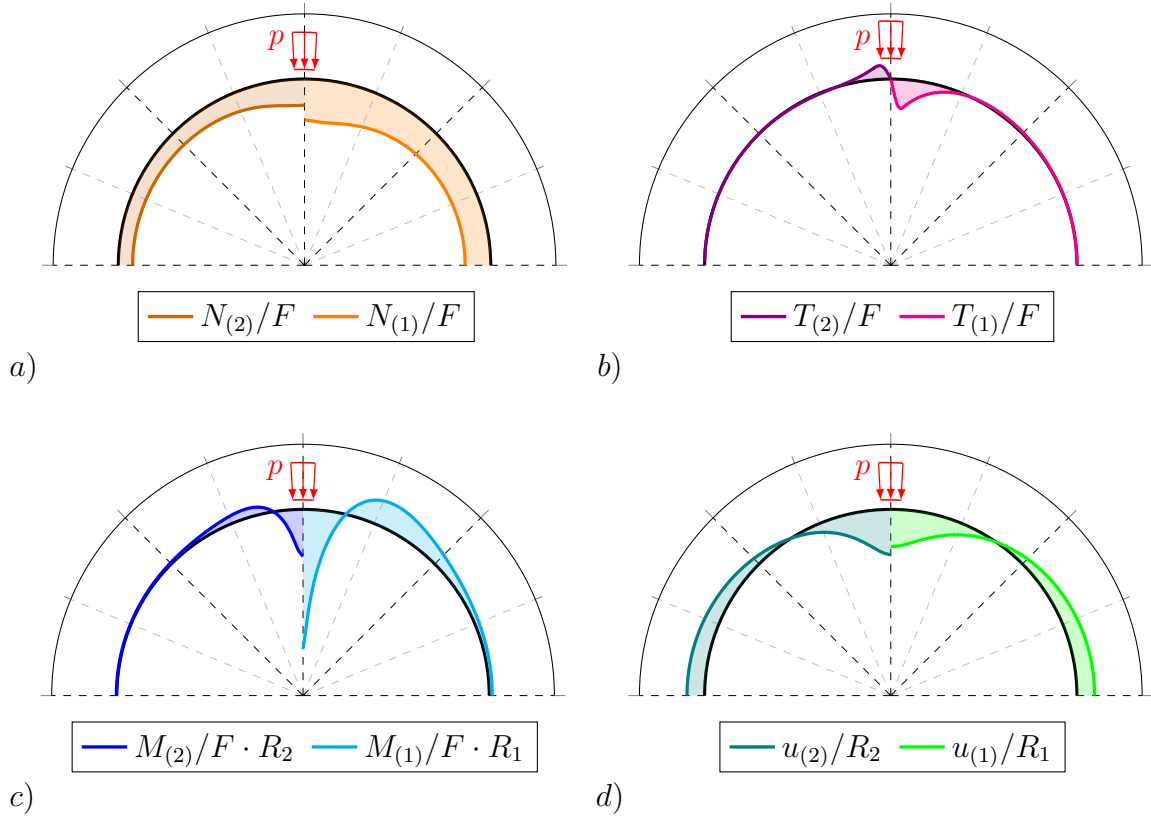


Figure 9: Force distributions and displacements of the coating for the two coated disks used in the experiments and loaded by two equal and opposite force distributions (reported in red, with resultant $F = 7\text{kN}$). The coatings are characterized by bending stiffness $EJ_1 = 1.4 \cdot 10^{-2} \text{ kNm}^2$ (index 1) and $EJ_2 = 7 \cdot 10^{-4} \text{ kNm}^2$ (index 2), representative of the samples reported on the left of Fig. 5. (a) Normalized normal forces $N_{(1)}/F$, $N_{(2)}/F$; (b) shear forces $T_{(1)}/F$, $T_{(2)}/F$; (c) normalized bending moments $M_{(1)}/(F \cdot R_1)$, $M_{(2)}/(F \cdot R_2)$, equations (81); (d) Normalized displacements $u_{(1)}/R_1$ and $u_{(2)}/R_2$, equation (77) along the external surface of the coated disk.

4.2.3 Special case: the disk with a coating imposing only an isoperimetric constraint, but not transmitting bending

At vanishing EJ for the coating, equation (49) reduces to the solution of a disk coated with a device (which may be imagined as an inextensible string) maintaining the isoperimetric constraint.

The determination of the elastic fields inside a disk coated with the above-mentioned axially inextensible constraint can be pursued by using equations (17) for the coated disk, in the limit for $EJ \rightarrow 0$. In particular, the Kolosov-Muskhelishvili potentials φ and ψ , equations (60)₁ and (61)₁, assume the same expressions (76) as for the coated case, but now the new coefficients A_{1-n}^{disk} for the disk without coating will be generated by requiring that the bending stiffness EJ in equation (49) vanishes

$$A_{1-n}^{disk} = \lim_{EJ \rightarrow 0} A_{1-n} = -\frac{\kappa R (n+1) \overline{D_n} + (n-1) D_n}{2\mu b (n-1)(n+\kappa n+\kappa-1)}, \quad \text{for } n \geq 2, \quad (82)$$

and hence potentials, equations (76), assume the form

$$\begin{aligned} \varphi^{disk}(z) &= -R \sum_{n=2}^{\infty} \left\{ \frac{(n-1) \overline{D_n} + (n+1) D_n}{b(n-1)(n+\kappa n+\kappa-1)} \right\} g^{-(n+1)}(z), \\ \psi^{disk}(z) &= R \sum_{n=2}^{\infty} \left\{ \frac{(n-1+\kappa) [(n-1) \overline{D_n} + (n+1) D_n]}{b(n-1)[(n+\kappa n+\kappa-1)]} \right\} g^{-(n-1)}(z). \end{aligned} \quad (83)$$

All the elastic fields which solve the problem of the disk with the isoperimetric coating without bending stiffness can now be computed through relations (17), with the substitutions $\varphi \rightarrow \varphi^{disk}$, $\psi \rightarrow \psi^{disk}$.

4.2.4 Stress distributions for different models of coating

Contour plots for the in-plane principal deviatoric stress $|\sigma_I - \sigma_{II}|$ and for the von Mises stress are reported inside the disk in Fig. 10, (a) and (b), respectively, both made dimensionless through division by the elastic shear modulus μ . Four models of disks are considered (only a quarter of the domain is reported), all loaded with the two radial compressive stress distributions shown in the figure. Results refer to: two coated disks, with (i.) $EJ_1 = 1.4 \cdot 10^{-2} \text{ kNm}^2$ and (ii.) $EJ_2 = 7 \cdot 10^{-4} \text{ kNm}^2$ (upper parts); (iii.) the disk coated with the isoperimetric constrain without bending stiffness; (iv.) the ‘nude’ disk, namely, unconstrained.

Note that the deviatoric and von Mises stress distributions are similar, as it may be expected as both are providing measures of distortional stress. Numbers reported on the contours facilitate comparisons and same colors refer to the same stress level.

The figure highlights the role of the bending stiffness of the coating, showing that the stress strongly increases at the mid point of load distribution, when the bending stiffness vanishes, as in the case of the isoperimetric constrained disk. This effect is even more pronounced in the case of the unconstrained disk. A non-local diffusion of the stresses are clearly visible in the coated cases.

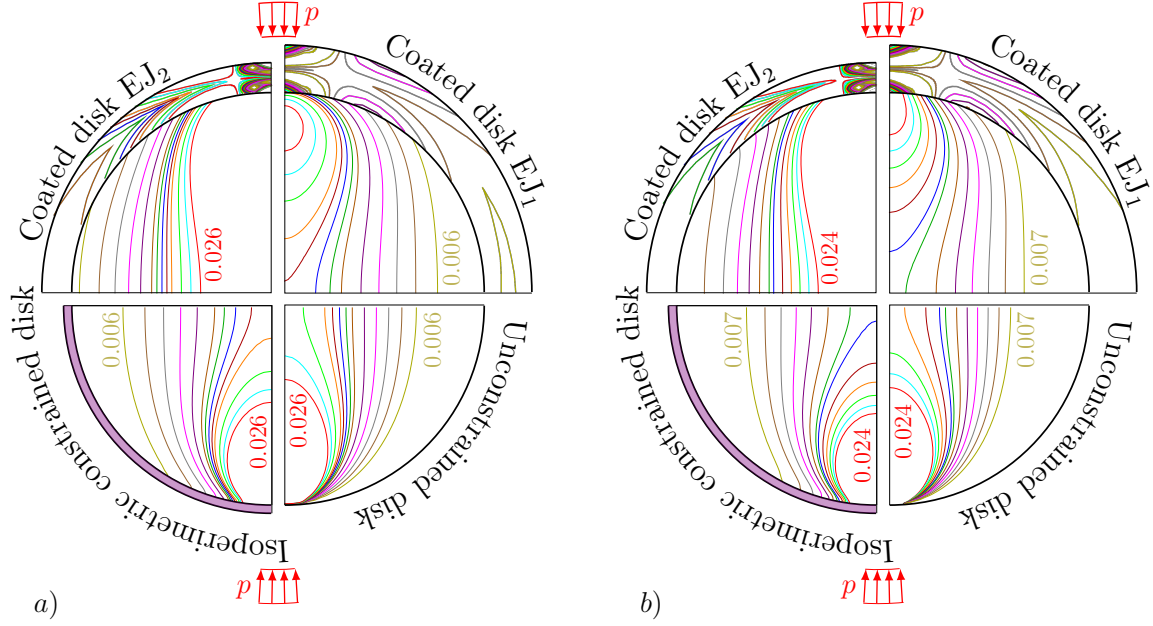


Figure 10: Various models of disks loaded under diametrical compression: with two coatings stiff under bending, EJ_1 , and EJ_2 ; with a coating imposing an isoperimetric constraint, but without bending stiffness; without any coating. Dimensionless stress contours for (a) in-plane deviatoric stress and (b) normalized von Mises stress are reported for disk and coating (sketched as a purple line when it corresponds to a mere isoperimetric constraint). The coating introduces a non local stress diffusion, an effect which tends to vanish when the bending stiffness of the coating is decreased, is strongly reduced for a disk with isoperimetric constraint, and vanishes when boundary constraints on the disk are absent.

4.3 Comparison between photoelastic experiments and mechanical modelling

4.3.1 Determination of stresses from fringe colours

The photoelastic analysis of the coated disk is reported below, referred to the same value of the load resultant $F = 7\text{kN}$, applied at the top of the vertical diameter of the samples shown in Fig. 5. Results are reported in Fig. 11, where the photoelastic image is reported on the right half of the sample, while the analytical solution is depicted on the left half. The in-plane deviatoric stress as determined from the analysis of the transmitted colours is reported in Table 3.

The stress field inside the disk shows an excellent agreement between theory and experiments, while the in-plane deviatoric stress in the external coating evidences some discrepancies. The latter are due to the fact that the coating has been modelled as an interface, so that the evaluation of the stresses is conducted starting from the knowledge of the internal force resultants, equations (81), using the classical de Saint-Venant theory, which is an approximation. Moreover, the stress level in the external part of the coating near the zone where the load is applied makes the reading of the transmitted colors difficult. For this reason, a quantitative evaluation of the stresses inside the external coating is not reported for the sample in the lower part of Fig. 5.

Although detachment is not possible in our experiments, points at the interface where

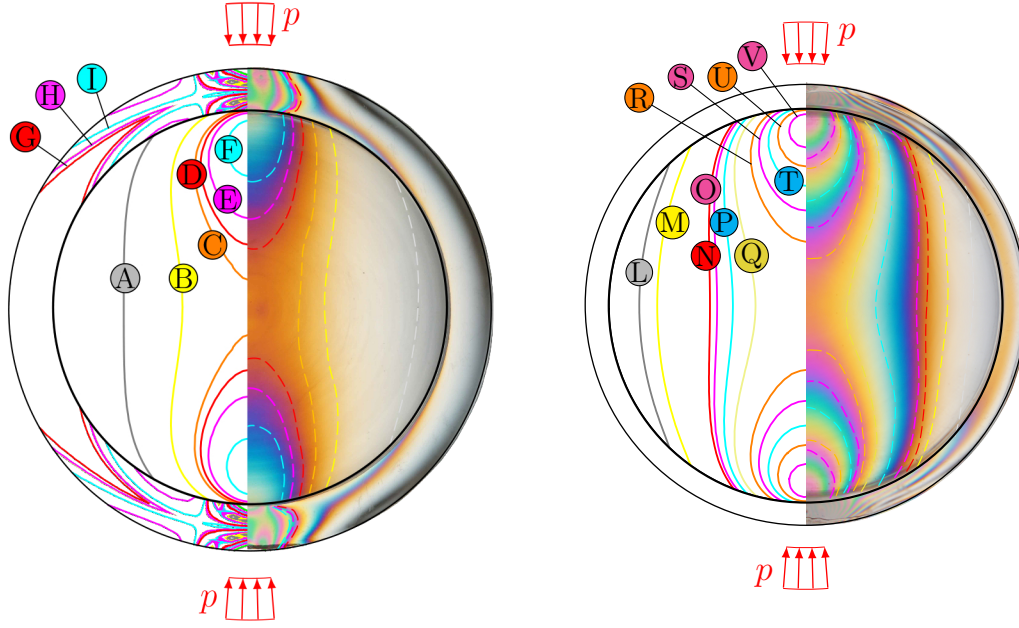


Figure 11: Determination of the in-plane deviatoric stress from the photoelastic fringes. The dashed lines on the right half of the sample refer to Table 3, while the location of the same stress level is reported on the left half of the sample, as evaluated with the analytic solution. The two samples are those reported in Fig. 5.

Transmitted color [–]	$N \cdot \lambda$ [nm]	Coated disk sample upper part of Fig. 5		Coated disk sample lower part of Fig. 5	
		Line [–]	$ \sigma_I - \sigma_{II} / \mu$ [–]	Line [–]	$ \sigma_I - \sigma_{II} / \mu$ [–]
Gray	1.218	A	0.0083	L	0.0083
Brilliant yellow	1.390	B	0.0148	M	0.0148
Orange	1.505	C	0.0192	-	-
Red	1.536	D	0.0203	N	0.0203
Indigo-violet	1.575	E	0.0219	O	0.0219
Sky blue	1.664	F	0.0252	P	0.0252
Brilliant Yellow	2.390	-	-	Q	0.0296
Orange	2.505	-	-	R	0.0384
Red	2.536	G	0.0108	-	-
Indigo-violet	2.575	H	0.0116	S	0.0438
Sky blue	2.664	I	0.0133	T	0.0505
Orange	3.505	-	-	U	0.0576
Indigo-violet	3.575	-	-	V	0.0657

Table 3: Determination of the in-plane deviatoric stress $|\sigma_I - \sigma_{II}| / \mu$ from the photoelastic experiments performed in the sample reported in the upper part of Fig. 5.

detachment between disk and coating may occur are those subject to tensile tractions. The distribution of the latter along the disk/coating interface are depicted in Fig. 12, where the two samples shown in Fig. 5 are subject to the resultant force $F = 7\text{kN}$. Note that red line refers to tensile tractions, while blue refers to compressive.

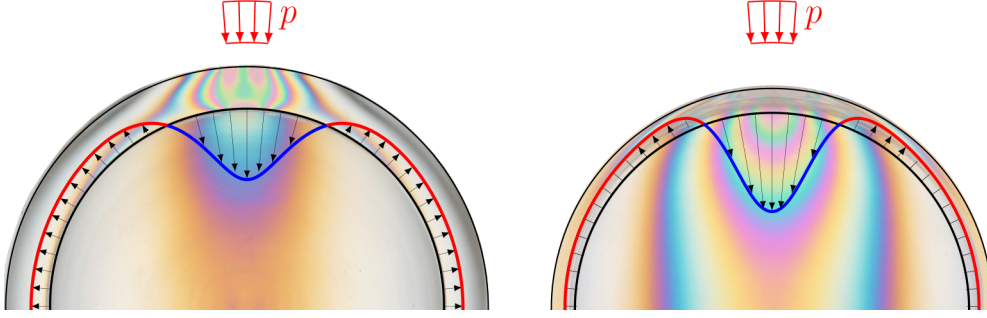


Figure 12: The traction applied to the disk is reported along the interface between coating and disk. When tensile (red line), the traction determines the zone where detachment of coating might occur (it does not in our experiments). The samples are those shown in Fig. 5.

5 Conclusions

Bulk materials having their external surface coated with a film of mechanical properties different from the base material are commonly used in a number of technologies. Within this context, a paradigmatic mechanical problem has been formulated in the present article, solved, and validated against experiments. This is a linear elastic (isotropic) circular disk, coated with a thin and stiff film, modelled as a linear elastic circular beam unshearable and axially inextensible, but linearly deformable under bending. The coating therefore imposes an isoperimetric constraint to the disk and a nonlocal load diffusion on its boundary. The latter effect is related to the introduction of an internal length scale and implies that concentrated forces applied to the external of the coating/disk complex do not introduce a singularity. It has been shown that the considered problem can be analytically solved via complex potentials formalism, so that the full displacement, strain, and stress fields have been derived for a generic applied external load. Finally, it has been shown how to practically realize the coated disk with a photoelastic material, thus producing two models which have been used to validate the analytical solution, in the case when two equal and opposed load distributions are applied on a small circular segment. The presented results open new possibilities in the design of coated solids of cylindrical geometry, which may find applications in micro and nano technologies, for instance in the characterization of nanowires via nanoindentation.

Acknowledgements

D.B. remembers with great pleasure and emotion the longstanding, intense, fruitful, and beautiful cooperation with Natasha and Sasha on so many topics of science. He looks forward to continue enjoying scientific collaboration with them and sincere friendship for many more years to come.

D.B. and M.G. gratefully acknowledges the funding from the European Union's Horizon 2020 research and innovation programme under the Marie Skłodowska-Curie grant agreement No 955944-REFRACTURE2. S.G.M. gratefully acknowledges support from National Science Foundation, award NSF CMMI - 2112894.

Appendices

Appendix A Calibration of the photoelastic model

Polimethyl Metacrilate, as other materials, exhibits the phenomenon known as *temporary birefringence* [51]. The photoelastic parameters for our experiments have been determined by testing under diametral compression a disk with radius $R = 35$ mm and thickness $b = 5$ mm. The usual identification of the photoelastic parameters is performed by using the elastic solution for a disk subject to opposite concentrated forces, for which the in-plane deviatoric stress $|\sigma_I - \sigma_{II}|$ at the centre of the disk is known [52]. In this way, the photoelastic constant f_σ of the material can be evaluated, once the fringe number N at the centre of the disk has been determined. From a photoelastic experiment performed on the uncoated disk (reported in the lower part of Fig. 5), the fringe number N appearing at the centre of the disk is found to be $N = 2$ from the left part of Fig. 13, referred to an applied force $F = 7.1$ kN. Therefore, the photoelastic constant of the material is found to be approximately $f_\sigma = 129.1$ N/mm.

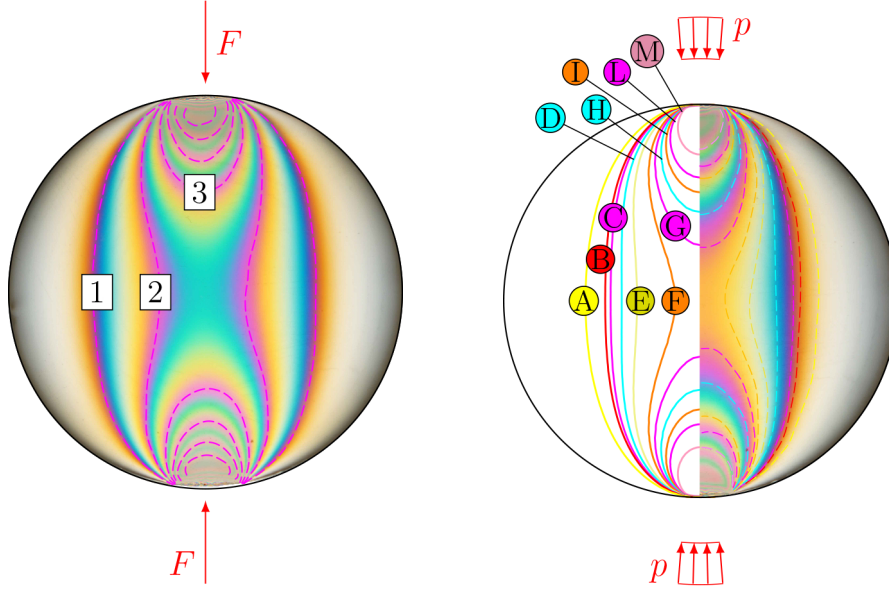


Figure 13: Left: A polymethyl methacrylate disk (subject to two opposite forces $F = 7.1$ kN) exhibits temporary birefringence displaying a fringe number $N = 2$ near the centre, where the corresponding indigo-violet fringes are visible. Right: the state of in-plane deviatoric stress (dashed line) compared with the theoretical results pertaining to the reported load distribution. Observation has been carried with a circular polariscope at a white light; quantitative results are reported in Table 4.

Having evaluated f_σ , the in-plane deviatoric stress inside the disk can be evaluated for each integer fringe number N (corresponding to indigo-violet transition colour, visible at a white light). In order to determine the order of fractional fringes, the in-plane deviatoric stress has to be evaluated for a particular transmitted colour, once its wave length λ is known. In Table 4 the dimensionless in-plane deviatoric stress for the coloured fringes are reported, as obtained during the photoelastic experiment shown in Fig. 13 (dashed line in the right part), contrasted with the analytic results (obtained for the sketched traction distribution and drawn as continuous lines) obtained from [49].

Line [–]	Transmitted colour [–]	$N\lambda$ [nm]	$ \sigma_I - \sigma_{II} /\mu$ [–]
A	Brilliant yellow	390	0.0148
B	Red	536	0.0203
C	Indigo-violet	575	0.0219
D	Sky blue	664	0.0252
E	Brilliant yellow	2·390	0.0296
F	Orange	2·505	0.0384
G	Indigo-violet	2·575	0.0438
H	Sky blue	2·664	0.0505
I	Orange	3·505	0.0576
L	Indigo-violet	3·575	0.0657
M	purple	4·565	0.0859

Table 4: Determination of the in-plane deviatoric stress $|\sigma_I - \sigma_{II}|/\mu$ from the photoelastic experiment performed in the uncoated disk sample reported in the lower part of Fig. 5.

Appendix B The ring, an annular beam

The problem of a loaded circular beam is a classical exercise in structural mechanics and can completely be solved by means of the relations (6), once the expressions for the radial displacement u_r in equation (25) is known in terms of the $A_{\pm n}$ coefficients. The stress distribution inside the circular beam can be determined once the internal forces have been determined from equations (81) in the limit $\mu \rightarrow 0$ for the disk.

Photoelastic experiments on the annular beams shown in Fig. 5 are reported in Fig. 14. The photos refer to four different compressive values of load, namely, 0.30 kN (0.06 kN), 0.40 kN (0.15 kN), 0.50 kN (0.30 kN), and 0.60 kN (0.40 kN) in the upper part (in the lower part). Maps of the normalized in-plane deviatoric stress $|\sigma_I - \sigma_{II}|/EJ$ are compared in Fig. 15 with the photoelastic experiments, loaded at 0.60 kN and 0.40 kN.

The results demonstrate the high accuracy of the beam theory to produce the stress distribution in a circular beam. This is a known result and can be found in [51].

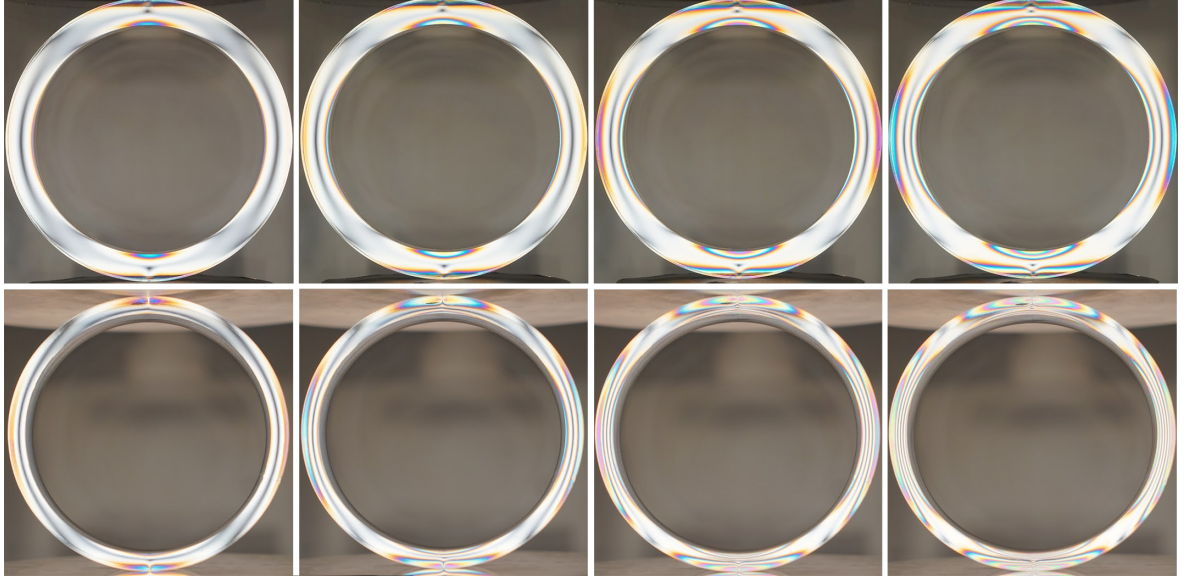


Figure 14: Photoelastic fringes generated during (vertical) diametrical compression of an annular beam, with bending stiffness $EJ_1=1.4 \cdot 10^{-2} \text{ kNm}^2$ (upper part) and $EJ_2=7 \cdot 10^{-4} \text{ kNm}^2$ (lower part). Four increasing values of compression are reported (from left to right): 0.30 kN (0.06 kN), 0.40 kN (0.15 kN), 0.50 kN (0.30 kN), and 0.60 kN (0.40 kN) in the upper part (in the lower part) for the samples shown in Fig. 5; photos have been taken at white circularly polarized light.

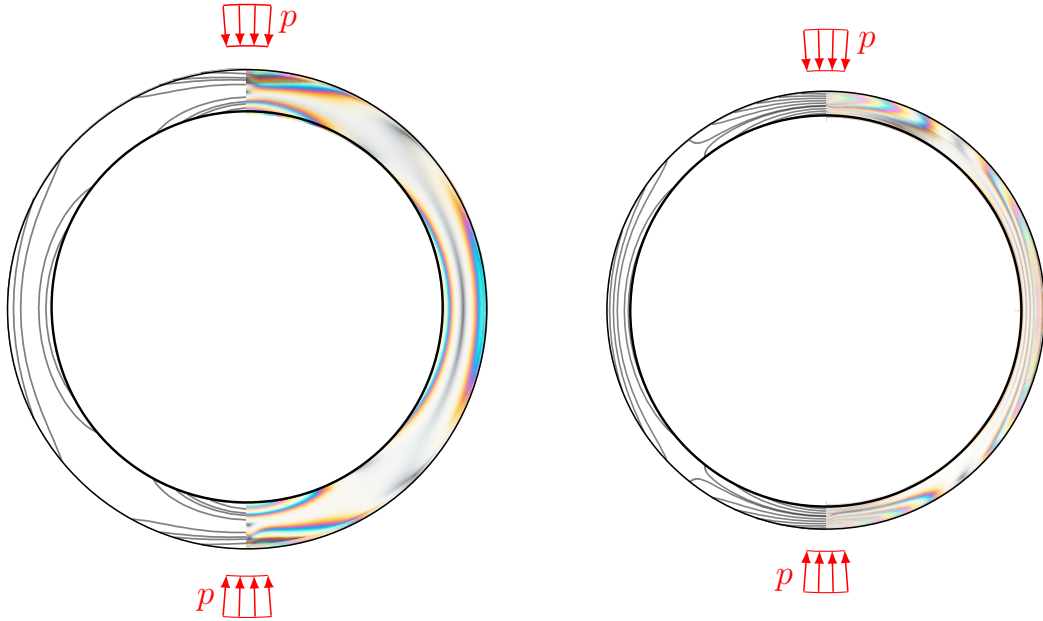


Figure 15: Distribution of the normalized in-plane deviatoric stress $(\sigma_I - \sigma_{II})/EJ_j$ ($j=1,2$) compared with the photoelastic fringes during a diametral compression test of two photoelastic circular beams with bending stiffness $EJ_1=1.4 \cdot 10^{-2} \text{ kNm}^2$ (left) and $EJ_2=7 \cdot 10^{-4} \text{ kNm}^2$ (right). The applied external load distribution p is modelled with a Fourier series expansion truncated at $N = 100$ and enhanced with the Lanczos smoothing method. The load distribution results in a compression of 0.60 kN (left) and 0.40 kN (right).

References

- [1] Y. Li, L. Zhao, and H. Shimizu, “Electrically conductive polymeric materials with high stretchability and excellent elasticity by a surface coating method,” *Macromolecular Rapid Communications*, vol. 32, no. 3, pp. 289–294, 2011.
- [2] H. Liang and R. G. Gordon, “Atmospheric pressure chemical vapor deposition of transparent conducting films of fluorine doped zinc oxide and their application to amorphous silicon solar cells,” *Journal of Materials Science*, vol. 42, no. 15, pp. 6388–6399, 2007.
- [3] L.-Y. Qi, L. Shang, X. Chen, L. Ye, W. Zhang, P. Feng, W. Zou, N. Cao, H.-H. Zhou, D. A. Weitz, *et al.*, “A versatile strategy to fabricate 3d conductive frameworks for lithium metal anodes,” *Advanced Materials Interfaces*, vol. 5, no. 19, p. 1800807, 2018.
- [4] R. Norizuki, T. Tanaka, E. Akahoshi, K. Kimura, K. Nakamura, and T. Chikada, “Fabrication and characterization of ceramic-iron joint coating for electrical insulation,” *Fusion Engineering and Design*, vol. 168, p. 112438, 2021.
- [5] C. Shen, H. Wang, T. Zhang, and Y. Zeng, “Silica coating onto graphene for improving thermal conductivity and electrical insulation of graphene/polydimethylsiloxane nanocomposites,” *Journal of Materials Science & Technology*, vol. 35, no. 1, pp. 36–43, 2019.
- [6] Z. Liu, H. Yang, Y. Jia, and X. Shu, “Heat protective properties of NiCrAlY/Al₂O₃ gradient ceramic coating fabricated by plasma spraying and slurry spraying,” *Surface and Coatings Technology*, vol. 327, pp. 1–8, 2017.
- [7] I. Zakirov, A. Nikulin, and N. Obabkov, “Study of the properties of ceramic heat-protective coatings applied on metal substances,” in *AIP Conference Proceedings 2015*, p. 020118, 2018.
- [8] Y. Oshida, A. Hashem, T. Nishihara, and M. Yapchulay, “Fractal dimension analysis of mandibular bones: toward a morphological compatibility of implants,” *Bio-medical Materials and Engineering*, vol. 4, no. 5, pp. 397–407, 1994.
- [9] E. Soldatova, E. Bolbasov, A. Kozelskaya, D. Kulbakin, N. Cherdyntseva, E. Choyazonov, and S. Tverdokhlebov, “Composite calcium phosphate coatings with hierarchical structure and antibacterial properties for maxillofacial surgery,” in *AIP Conference Proceedings*, vol. 2310, p. 020324, 2020.
- [10] T. Suzuki, N. Hori, W. Att, K. Kubo, F. Iwasa, T. Ueno, H. Maeda, and T. Ogawa, “Ultraviolet treatment overcomes time-related degrading bioactivity of titanium,” *Tissue Engineering Part A*, vol. 15, no. 12, pp. 3679–3688, 2009.
- [11] O. Tokariev, T. Van Gestel, M. Bram, and J. Malzbender, “Strength enhancement of transparent spinel ceramics,” *Materials Letters*, vol. 107, pp. 364–366, 2013.
- [12] C. Jinlong, Y. Xuefeng, W. Shouren, Z. Hui, Y. Liying, Q. Yang, and L. Chenchen, “Wear and corrosion resistance of laser cladding ni60-tic ceramic coating on 45 steel surface,” *Rare Metal Materials and Engineering*, vol. 49, no. 2, pp. 611–617, 2020.

- [13] M. E. Gurtin and A. I. Murdoch, “A continuum theory of elastic material surfaces,” *Archive for Rational Mechanics and Analysis*, vol. 57, no. 4, pp. 291–323, 1975.
- [14] D. J. Steigmann and R. W. Ogden, “Elastic surface—substrate interactions,” *Proceedings of the Royal Society of London. Series A: Mathematical, Physical and Engineering Sciences*, vol. 455, no. 1982, pp. 437–474, 1999.
- [15] D. Steigmann and R. Ogden, “Plane deformations of elastic solids with intrinsic boundary elasticity,” *Proceedings of the Royal Society of London. Series A: Mathematical, Physical and Engineering Sciences*, vol. 453, no. 1959, pp. 853–877, 1997.
- [16] D. Bigoni, N. Bordinon, A. Piccolroaz, and S. Stupkiewicz, “Bifurcation of elastic solids with sliding interfaces,” *Proceedings of the Royal Society A: Mathematical, Physical and Engineering Sciences*, vol. 474, no. 2209, p. 20170681, 2018.
- [17] G. Dryburgh and R. Ogden, “Bifurcation of an elastic surface-coated incompressible isotropic elastic block subject to bending,” *Zeitschrift für angewandte Mathematik und Physik ZAMP*, vol. 50, no. 5, pp. 822–838, 1999.
- [18] M. Gei and R. W. Ogden, “Vibration of a surface-coated elastic block subject to bending,” *Mathematics and Mechanics of Solids*, vol. 7, no. 6, pp. 607–628, 2002.
- [19] Y. Benveniste, G. Dvorak, and T. Chen, “Stress fields in composites with coated inclusions,” *Mechanics of Materials*, vol. 7, no. 4, pp. 305–317, 1989.
- [20] Y. Benveniste and T. Miloh, “Imperfect soft and stiff interfaces in two-dimensional elasticity,” *Mechanics of Materials*, vol. 33, no. 6, pp. 309–323, 2001.
- [21] Y. Benveniste, “The effective mechanical behaviour of composite materials with imperfect contact between the constituents,” *Mechanics of Materials*, vol. 4, no. 2, pp. 197–208, 1985.
- [22] D. Bigoni and A. Movchan, “Statics and dynamics of structural interfaces in elasticity,” *International Journal of Solids and Structures*, vol. 39, no. 19, pp. 4843–4865, 2002.
- [23] T. Miloh and Y. Benveniste, “On the effective conductivity of composites with ellipsoidal inhomogeneities and highly conducting interfaces,” *Proceedings of the Royal Society of London. Series A: Mathematical, Physical and Engineering Sciences*, vol. 455, no. 1987, pp. 2687–2706, 1999.
- [24] J. W. Suk, R. D. Piner, J. An, and R. S. Ruoff, “Mechanical properties of monolayer graphene oxide,” *ACS nano*, vol. 4, no. 11, pp. 6557–6564, 2010.
- [25] Y. Wei and R. Yang, “Nanomechanics of graphene,” *National Science Review*, vol. 6, no. 2, pp. 324–348, 2019.
- [26] S. Mogilevskaya, S. Crouch, and H. Stolarski, “Multiple interacting circular nano-inhomogeneities with surface/interface effects,” *Journal of the Mechanics and Physics of Solids*, vol. 56, no. 6, pp. 2298–2327, 2008.

- [27] Z. Han, S. G. Mogilevskaya, and D. Schillinger, “Local fields and overall transverse properties of unidirectional composite materials with multiple nanofibers and Steigmann–Ogden interfaces,” *International Journal of Solids and Structures*, vol. 147, pp. 166–182, 2018.
- [28] S. G. Mogilevskaya, A. Y. Zemlyanova, and M. Zammarchi, “On the elastic far-field response of a two-dimensional coated circular inhomogeneity: Analysis and applications,” *International Journal of Solids and Structures*, vol. 130, pp. 199–210, 2018.
- [29] S. Baranova, S. Mogilevskaya, V. Mantič, and S. Jiménez-Alfaro, “Analysis of the antiplane problem with an embedded zero thickness layer described by the Gurtin–Murdoch model,” *Journal of Elasticity*, vol. 140, no. 2, pp. 171–195, 2020.
- [30] S. G. Mogilevskaya, A. Y. Zemlyanova, and V. Mantič, “The use of the gurtin-murdoch theory for modeling mechanical processes in composites with two-dimensional reinforcements,” *Composites Science and Technology*, vol. 210, p. 108751, 2021.
- [31] J. W. Hutchinson and Z. Suo, “Mixed mode cracking in layered materials,” *Advances in Applied Mechanics*, vol. 29, pp. 63–191, 1991.
- [32] O. Jørgensen, A. Horsewell, B. Sørensen, and P. Leisner, “The cracking and spalling of multilayered chromium coatings,” *Acta Metallurgica et Materialia*, vol. 43, no. 11, pp. 3991–4000, 1995.
- [33] Z. Suo and J. W. Hutchinson, “Steady-state cracking in brittle substrates beneath adherent films,” *International Journal of Solids and Structures*, vol. 25, no. 11, pp. 1337–1353, 1989.
- [34] J. Beuth Jr, “Cracking of thin bonded films in residual tension,” *International Journal of Solids and Structures*, vol. 29, no. 13, pp. 1657–1675, 1992.
- [35] G. Gioia and M. Ortiz, “Delamination of compressed thin films,” *Advances in Applied Mechanics*, vol. 33, no. 8, pp. 119–192, 1997.
- [36] M. Y. He, A. G. Evans, and J. W. Hutchinson, “Crack deflection at an interface between dissimilar elastic materials: role of residual stresses,” *International Journal of Solids and Structures*, vol. 31, no. 24, pp. 3443–3455, 1994.
- [37] M. Hu, M. D. Thouless, and A. G. Evans, “The decohesion of thin films from brittle substrates,” *Acta Metallurgica*, vol. 36, no. 5, pp. 1301–1307, 1988.
- [38] H. M. Jensen, J. W. Hutchinson, and K. Kyung-Suk, “Decoherence of a cut prestressed film on a substrate,” *International Journal of Solids and Structures*, vol. 26, no. 9-10, pp. 1099–1114, 1990.
- [39] H. M. Jensen and I. Sheinman, “Numerical analysis of buckling-driven delamination,” *International Journal of Solids and Structures*, vol. 39, no. 13-14, pp. 3373–3386, 2002.
- [40] Z. Suo and J. W. Hutchinson, “Interface crack between two elastic layers,” *International Journal of Fracture*, vol. 43, no. 1, pp. 1–18, 1990.

- [41] H.-H. Yu, M. He, and J. Hutchinson, “Edge effects in thin film delamination,” *Acta Materialia*, vol. 49, no. 1, pp. 93–107, 2001.
- [42] H.-h. Yu and J. W. Hutchinson, “Delamination of thin film strips,” *Thin Solid Films*, vol. 423, no. 1, pp. 54–63, 2003.
- [43] T. Q. Lu, W. X. Zhang, and T. Wang, “The surface effect on the strain energy release rate of buckling delamination in thin film–substrate systems,” *International Journal of Engineering Science*, vol. 49, no. 9, pp. 967–975, 2011.
- [44] K. Wu, J. Zhang, G. Liu, P. Zhang, P. Cheng, J. Li, G. Zhang, and J. Sun, “Buckling behaviors and adhesion energy of nanostructured Cu/X (X= Nb, Zr) multilayer films on a compliant substrate,” *Acta Materialia*, vol. 61, no. 20, pp. 7889–7903, 2013.
- [45] L. Zhuo and Y. Zhang, “The mode-coupling of a stiff film/compliant substrate system in the post-buckling range,” *International Journal of Solids and Structures*, vol. 53, pp. 28–37, 2015.
- [46] G. Wang, Z. He, and Q. Chen, “The surface effects on solid and hollow nanowires under diametral loading,” *Applied Mathematical Modelling*, vol. 96, pp. 697–718, 2021.
- [47] H. Qi, K. Teo, K. Lau, M. Boyce, W. Milne, J. Robertson, and K. Gleason, “Determination of mechanical properties of carbon nanotubes and vertically aligned carbon nanotube forests using nanoindentation,” *Journal of the Mechanics and Physics of Solids*, vol. 51, no. 11-12, pp. 2213–2237, 2003.
- [48] S. Timoshenko, *Strength of Materials: Pt. 1. Elementary Theory and Problems*, vol. 1. Van Nostrand, 1940.
- [49] N. Muskhelishvili, *Some basic problems of the mathematical theory of elasticity*. Springer Science & Business Media, 1959.
- [50] A. Zemlyanova and S. Mogilevskaya, “Circular inhomogeneity with Steigmann–Ogden interface: Local fields, neutrality, and Maxwell’s type approximation formula,” *International Journal of Solids and Structures*, vol. 135, pp. 85–98, 2018.
- [51] M. M. Frocht, *Photoelasticity*, vol. 2. J. Wiley and Sons, 1965.
- [52] W. Dally and W. Riley, “Experimental stress analysis.” *New York: College House Enterprises, LLC*, 1991.